

High Current Density in Monolayer MoS₂ Doped by AlO_x

Connor J. McClellan¹, Eilam Yalon^{1,2}, Kirby K.H. Smithe¹, Saurabh V. Suryavanshi¹, and Eric Pop^{1,3,*}

¹*Electrical Engineering, Stanford University, Stanford, CA 94305, USA.*

²*Present address: Electrical Engineering, Technion, Israel Institute of Technology, Haifa, 32000, Israel*

³*Materials Science and Engineering, Stanford University, Stanford, CA 94305, USA.*

ABSTRACT: Semiconductors require stable doping for applications in transistors, optoelectronics, and thermoelectrics. However, this has been challenging for two-dimensional (2D) materials, where existing approaches are either incompatible with conventional semiconductor processing or introduce time-dependent, hysteretic behavior. Here we show that low temperature (< 200°C) sub-stoichiometric AlO_x provides a stable *n*-doping layer for monolayer MoS₂, compatible with circuit integration. This approach achieves carrier densities >2×10¹³ cm⁻², sheet resistance as low as ~7 kΩ/□, and good contact resistance ~480 Ω·μm in transistors from monolayer MoS₂ grown by chemical vapor deposition. We also reach record current density of nearly 700 μA/μm (>110 MA/cm²) in this three-atom-thick semiconductor while preserving transistor on/off current ratio > 10⁶. The maximum current is ultimately limited by self-heating and could exceed 1 mA/μm with better device heat sinking. With their 0.1 nA/μm off-current, such doped MoS₂ devices approach several low-power transistor metrics required by the international technology roadmap.

KEYWORDS: 2D semiconductors, current density, doping, high-field, self-heating, MoS₂, Al₂O₃

The success of modern electronics has relied on conventional silicon transistor scaling, enabling advancements in computing technology year after year for over five decades. Recent field-effect transistors (FETs) have used top-down fabrication to realize ultrathin silicon “fins” (*i.e.* FinFETs)^{1,2} for improved control of leakage current and performance. However, these approaches have limitations imposed by process variation and the degradation of silicon mobility in ultrathin, approximately sub-4 nm layers.³ The emergence of sub-1 nm thin monolayer 2D semiconductors could therefore extend transistor scaling, representing the ultimate limit of semiconductors, without an analogue among bulk materials like silicon.⁴ For example, monolayer 2D semiconductors like MoS₂ could enable sub-5 nm scale transistors⁵ and, owing to their direct band gap, could also allow integration with optoelectronic devices.⁶ Recent research has demonstrated the integration properties of monolayer 2D semiconductors, including three-dimensional (3D) monolithic systems⁷ and flexible electronics.⁸

However, the atomic thinness of 2D semiconductors has raised questions about the ability to dope them and, consequently, about their ultimate performance in integrated circuits. While doping bulk materials like silicon is achieved with substitutional impurities, such an approach in a three-atom-thick material could significantly degrade the mobility. In addition, performance cannot only be judged based on (low-field) mobility, but also on the maximum drive current I_{on} , because circuit delays are proportional to CV/I_{on} , where C is the capacitance including parasitics and V is the voltage. To meet International Roadmap of Devices and Systems (IRDS)⁹ specifications for low-power transistors, the on-state current must exceed $I_{\text{on}} > 480 \mu\text{A}/\mu\text{m}$, while the off-state current must remain $I_{\text{off}} < 0.1 \text{ nA}/\mu\text{m}$, ideally within a narrow voltage swing (e.g. 0.7 or 1 V) for low-power operation.

Past studies of doping 2D materials have explored surface functionalization of acceptor^{10,11} or donor¹² states, but a large degradation in transistor subthreshold swing (SS) was often observed due to induced trap states. Chemical charge transfer doping was also proposed,^{13,14} however such approaches face stability and integration issues. Instead, sub-stoichiometric metal oxides (like MoO_x for p -type¹⁵ and AlO_x or TiO_x for n -type^{16,17}) have been used as *stable* doping layers of 2D materials, but doped devices typically experience a severe reduction in on/off current ratio ($I_{\text{on}}/I_{\text{off}}$) and poor SS . Such challenges have ultimately prevented the achievement of 2D transistors with high on-current and good $I_{\text{on}}/I_{\text{off}}$. Furthermore, most doping studies on 2D semiconductors have been limited to thicker, multi-layer semiconductors,^{13,18} which have no clear technological benefit over ultrathin silicon-on-insulator (SOI) or FinFETs,^{1,19} far more mature technologies.

In this work, we demonstrate a stable doping approach that preserves the transistor $I_{\text{on}}/I_{\text{off}}$, while enabling record-high I_{on} , record-low sheet resistance, and low contact resistance in a three-atom-thick semiconductor. These results are enabled by the increase in carrier concentration from doping while maintaining a low interface trap density through annealing. Importantly, this is achieved with MoS_2 grown by large-area chemical vapor deposition (CVD),²⁰ which is necessary for practical applications. Our three-atom-thick MoS_2 transistors reach $I_{\text{on}} \approx 700 \mu\text{A}/\mu\text{m}$ at 5 V ($\sim 300 \mu\text{A}/\mu\text{m}$ at 1 V) while maintaining $I_{\text{off}} < 0.1 \text{ nA}/\mu\text{m}$. These achievements advance monolayer semiconductors to an important position for low-power logic and memory, approaching industrial specifications.

RESULTS AND DISCUSSION

Device Design: Figure 1a shows the schematic of our transistors fabricated using monolayer MoS_2 grown by CVD directly onto SiO_2 ($t_{\text{ox}} = 30 \text{ nm}$) on p^{++} Si, which also serves as a back-gate, with pure Au contacts²¹ (also see Methods). The uncapped (and undoped) monolayer MoS_2 has a field-effect

mobility of 35 to 40 $\text{cm}^2\text{V}^{-1}\text{s}^{-1}$ in this work, which could range from 30 to 50 $\text{cm}^2\text{V}^{-1}\text{s}^{-1}$ in our previous studies on similar CVD-grown material.²⁰ To dope these, we first use electron beam evaporation to deposit a thin 1 nm Al seed layer that immediately oxidizes upon air exposure to form sub-stoichiometric AlO_x , followed by 15 nm of AlO_x deposited by atomic layer deposition (ALD), and additional details are given in Methods. Figure 1b displays an atomic force microscopy (AFM) image of multiple such MoS_2 devices in a transfer length method (TLM) structure with channel lengths from $L = 180$ to 980 nm, as measured. For good contact resistance (R_c) estimates, such TLM structures must include channel lengths ranging from “short” (dominated by their contacts) to “long” (dominated by the channel resistance).²¹ Extrapolating R_c only from long channel devices could lead to large uncertainty and even apparently negative contact resistance from TLM extractions.²² The corresponding photoluminescence (PL) and Raman spectra of these channels before and after AlO_x -capping are displayed in Figs. 1c and 1d, respectively, and additional details are provided in Supporting Section S1.

Doping vs. Trapping Induced by the Oxide: Before presenting the electrical data, we note that doping the 2D material by metal oxides can result from at least two distinct processes. In the first process the charge is induced by trap states at the semiconductor/oxide interface (classically referred to as D_{it}) or in the oxide near the interface (*e.g.* border traps).^{23,24} These traps are energetically located within the energy gap of the 2D semiconductor and ultimately lead to degradation of mobility or SS . The other process for doping the 2D material is by transfer of electrons or holes from states that do not overlap with the energy gap of the 2D semiconductor, analogous to modulation doping in high electron mobility transistors (HEMTs).²⁵ Similar effects have been attributed to dipoles in high- k dielectrics on Si transistors, where dipoles affect the mobile carrier density in the channel.²⁶ In this case, the induced charge carriers end up in the conduction (valence) band for n -type (p -type) doping, and do not degrade the SS or mobility of the 2D transistor. Such techniques are commonly used in the semiconductor industry to adjust the threshold voltage (V_T) in Si transistors, utilizing either fixed charge or dipoles.²⁷

Figures 2a,b show measured linear and logarithmic drain current *vs.* gate voltage of a 3 μm long MoS_2 channel before AlO_x deposition (gray), immediately after AlO_x doping (light red), and after an anneal in N_2 at 200°C for 40 minutes (dark red). Note that all I - V measurements shown here include forward and backward sweeps, as labeled by small arrows, while the minimum and maximum gate voltages are limited by the breakdown field of the gate dielectric. Immediately after ALD of AlO_x the carrier and current density increase, but the SS and transconductance ($g_m = \partial I_D / \partial V_{GS}$) degrade, indicating the as-deposited AlO_x leads to carrier trapping. The induced trap density is high, $\Delta D_{it} \sim 5 \times 10^{13} \text{ cm}^{-2}\text{eV}^{-1}$ estimated from the change in SS (Supporting Section S2). However, after annealing in N_2 the

SS , mobility, and g_m recover to their values measured in the undoped channel, with a negative V_T shift corresponding to $\sim 8.6 \times 10^{12} \text{ cm}^{-2}$ electron doping (Supporting Section S5), and a current increase by $>50\%$ at the highest V_{GS} shown. The sheet resistance of this long channel after doping and annealing is the lowest reported to date, $R_{sh} \approx 7 \text{ k}\Omega/\square$, estimated after subtracting the small ($<4\%$) contribution of the contact resistance discussed below.

The trapping and doping states observed in Figs. 2a,b are linked to AlO_x defects and their energy distribution at or near the $\text{AlO}_x/\text{MoS}_2$ interface.²⁸⁻³⁰ Figure 2c displays an energy band diagram of the doping effect, showing three defect states in AlO_x modeled previously using density functional theory (DFT),³⁰ originating from oxygen vacancies in sub-stoichiometric AlO_x . These defect states each have a charge and energy level that depend on the electron occupation. Defects with high electron occupation have lower energy levels and no charge (D^0), whereas removing electrons raises the defect energy level and leaves positive charge. The change in defect energy level from removing or adding electrons has been shown with DFT to occur from redistribution of the surrounding atoms in the metal oxide, changing the required energy to add or remove an electron, respectively.²⁸⁻³⁰

Shallow defects that have energy levels within the MoS_2 band gap and available electron states (D^{1+}) lead to trapping of MoS_2 channel electrons, decreasing their mobility because the localized electrons “hop” between defects.³¹ If the defects donate their electrons and reside at energy levels above the MoS_2 conduction band (D^{2+}), the MoS_2 electrons are not trapped. These higher energy defect states donate electrons and become positively charged, inducing negative (mobile) charge in the MoS_2 channel. Remote Coulomb scattering with these charged D^{2+} states could limit the channel mobility, as is the case for HEMTs,³² but this is not observed here as the MoS_2 mobility after AlO_x capping and anneal is virtually unchanged from the uncapped samples. This indicates that such remote Coulomb scattering is either screened by the AlO_x or that the MoS_2 mobility is more strongly limited by intrinsic defects and phonons in our samples.³³

Using the Stanford 2D Semiconductor (S2DS) FET model,³⁴ we successfully simulate the data in Fig. 2b. The model can describe both the sub-threshold (diffusion) and above-threshold (drift) current components, with additional details in Supporting Section S3. The large degradation of SS immediately after AlO_x deposition is due to mid-gap defects, included in the model as an interface capacitance ($C_{it} = q^2 D_{it}$)²⁷ which reduces the overall gate capacitance ($1/C_G = 1/C_{ox} + 1/C_{it}$) where $C_{ox} = \epsilon_{ox}/t_{ox}$, ϵ_{ox} and t_{ox} being the permittivity and thickness of the SiO_2 , respectively. Thus $C_G < C_{ox}$, which can lead to an overestimation of carrier density and underestimation of mobility (Supporting Section S3).

The good agreement between the experimental data and the D_{it} model shows how trapping and doping can be induced by changing the energy level and defects density in the AlO_x . Annealing in a non-reactive, inert N_2 ambient^{35,36} after AlO_x deposition helps promote the defects to donate electrons to the MoS_2 , analogous to dopant activation steps in conventional semiconductors. These results highlight the difference between trapping and doping of mobile charge in 2D materials. Here we achieve 2D doping without degradation of I_{on}/I_{off} , unlike previous studies where the decreased I_{on}/I_{off} was (incorrectly) attributed to large doping, although this was likely a D_{it} effect.

We also fabricated long channel ($L = 6 \mu\text{m}$) top-gated MoS_2 FETs using the AlO_x as the top gate insulator (Supporting Section S4). As expected, we found that after anneal (the doping state), the AlO_x enables good electrostatic control and low gate leakage, evidence of an insulating oxide. However, before anneal (in the AlO_x trapping state) the top gate control was weak and the gate leakage current was much higher (see Supporting Section S4). The leaky AlO_x in the trapping state is consistent with defect states within the MoS_2 band gap, which lead to trap-assisted tunneling and gate leakage.

We have analyzed other sub-stoichiometric oxides for doping 2D materials in previous studies, including MoO_3 (for p -doping WSe_2 and graphene),^{15,37} as well as TiO_x and NiO_x .³⁸ However, we have found that AlO_x provides the best results for n -type doping likely due to the Al seed not reacting with nor damaging MoS_2 . In contrast, Ti and Ni can react with and damage monolayer MoS_2 ,³⁸ respectively, leading to lower mobility.

Contact and Sheet Resistance: To obtain the contact resistance of the doped MoS_2 , we use TLM structures²¹ from Fig. 1b and measure resistance vs. length (Fig. S5). Figure 3a displays the effective mobility (μ_{eff} , here an average over the six channels) from the sheet resistance, before and after the N_2 anneal. The mobility increases from $12.8 \text{ cm}^2\text{V}^{-1}\text{s}^{-1}$ before the anneal (due to the large D_{it}) to $33.5 \text{ cm}^2\text{V}^{-1}\text{s}^{-1}$ after the anneal, similar to that of our undoped monolayer MoS_2 .²⁰ The average sheet resistance is $R_{sh} = 9.0 \pm 0.5 \text{ k}\Omega/\square$ at $n \approx 2 \times 10^{13} \text{ cm}^{-2}$ in this TLM and $\sim 7 \text{ k}\Omega/\square$ in the doped long-channel device of Fig. 2a. These are the lowest sheet resistances observed to date for monolayer MoS_2 at room temperature, comparable to those achieved using superionic conductor (LaF_3) gating at the lower temperature of 220 K.³⁹ Figure 3b shows the contact resistance vs. n , reaching as low as $R_C \approx 480 \Omega \cdot \mu\text{m}$ for Au with monolayer MoS_2 after AlO_x doping. This is also the lowest contact resistance to any CVD-grown monolayer semiconductor and one of the lowest amongst all 2D semiconductors.^{16,40}

We attribute the low R_C to the reduction in Schottky barrier width between Au and MoS_2 with increased carrier concentration, although the AlO_x doping layer only touches the edge of the contact.

This reduction in R_C from channel doping has been observed before^{15,16} and can be attributed to two causes. First, as the R_{sh} of the metal is far less than that of the 2D material, the current transfer length ≈ 50 nm (*i.e.* region of current injection under the contact, see Supporting Section S5), leading to most of the current being injected very close to the contact edge.^{41,42} Second, due to the 2D nature of the channel, the depletion region of the Schottky contact extends beyond the contact edge into the channel.⁴¹ As a result, increasing the carrier density by AlO_x doping at or near the edge of the metal contact reduces the Schottky depletion region, increasing tunneling from metal to semiconductor as is observed in highly doped Si/metal contacts. This is further evidenced by comparing this result to our previous R_C results in MoS_2 devices,^{21,43} as shown in Figure 3b, where the new reduction in R_C is achieved by reaching higher carrier densities through the use of AlO_x doping.

The low R_C and R_{sh} in our monolayer MoS_2 allow us to reach a maximum current $I_{on} \approx 690 \mu\text{A}/\mu\text{m}$ in a 380 nm long channel at $V_{DS} = 5$ V (Fig. 3c), achieving a record current density $J_{on} > 110 \text{ MA}/\text{cm}^2$ for the three-atom-thick MoS_2 with $t_{ch} = 6.15 \text{ \AA}$.⁴⁴ This current density is the highest recorded to date in a 2D semiconductor, approximately $5\times$ higher than the typical electromigration current densities of common metals and surpassed only by that of graphene (a 2D semimetal)⁴⁵ and carbon nanotubes⁴⁶ which are near $\sim 1 \text{ GA}/\text{cm}^2$. Strictly speaking, this device reaches $I_D \approx 300 \mu\text{A}/\mu\text{m}$ at $V_{DS} = 1$ V and the IRDS low-power specification⁹ ($> 480 \mu\text{A}/\mu\text{m}$) is met at $V_{DS} = 2$ V. To meet this at ≤ 1 V would require a two-fold improvement in mobility or a combined increase in mobility and carrier density, coupled with a reduction of contact resistance. We also keep in mind that the device shown in Fig. 3c has $L = 380$ nm, whereas the IRDS specifications⁹ are meant for FETs of 10-20 nm channel length.

Figure 3d shows the transfer characteristics of the same transistor, demonstrating stable doping with only slight degradation after 60 days in air, and negligible hysteresis (both forward and backward measurement sweeps are shown). The device can turn off to $0.1 \text{ nA}/\mu\text{m}$ and exhibits $I_{on}/I_{off} \approx 2.5 \times 10^6$ despite the high doping even at $V_{DS} = 5$ V (Supporting Section S6), contrasting other doped 2D material transistors where the high on-state current was only achieved with low on/off ratio. These metrics are comparable to or better than those of recent silicon-on-insulator (SOI) devices,⁴⁷ yet achieved in a ~ 16 times thinner monolayer MoS_2 channel, and additional comparisons are provided in the Benchmarking section below. We emphasize that reaching high on-current density while preserving SS and sufficient I_{on}/I_{off} is a critical figure of merit to benchmark practical doping techniques of 2D materials.

Current Density Limits: Despite the record current density achieved here in a three-atom-thick semiconductor, it is important to ask what is limiting the maximum current and whether this could be

improved further, given that high current (per transistor width) is required for high speed circuit operation. With a fixed parasitic resistance of $960 \text{ } \Omega \cdot \mu\text{m}$ ($= 2R_C$) and channel resistance of $300 \text{ } \Omega \cdot \mu\text{m}$, our devices could reach $600 \text{ } \mu\text{A}/\mu\text{m}$ at 20 nm gate lengths and $V_{DS} = 0.75 \text{ V}$, meeting IRDS low-power specifications.⁹ In comparison, state of the art Si or III-V transistors can reach $>1 \text{ mA}/\mu\text{m}$,^{1,48} but in much “thicker” channels.

The maximum current density of a transistor is limited by mobility or saturation velocity, carrier density, contact resistance, and self-heating during operation. Naturally, higher mobility (such as in III-V semiconductors or graphene) automatically leads to higher current density, but high carrier density can compensate for a lower-mobility semiconductor (as in this work). Shorter channel transistors can also reach higher operating currents, down to channel lengths that are limited by their contact resistance and injection velocity.⁴⁹ However, with a “given” set of material and contact parameters, we find that self-heating ultimately limits the maximum current achieved in our devices.

To understand this, we turn to Fig. 4, which compares our measurements (symbols) with simulations (lines) including velocity saturation,⁴³ contact resistance, and self-heating effects (further details provided in Supporting Section S7). By including these effects, our simulations capture the deviation from linearity in Fig. 4A, at high drain bias $V_{DS} > 2 \text{ V}$. These devices heat up significantly during measurement due to the high current density and relatively high thermal resistance of the MoS_2 - SiO_2 interface and the SiO_2 substrate.⁵⁰ Consequently, as the input power ($P = I_D V_{DS}$) increases, the temperature rise ΔT degrades the carrier mobility and saturation velocity. We estimate a $\Delta T \sim 400 \text{ K}$ channel temperature rise at the highest bias point probed here, with heat flow being limited by the relatively low thermal boundary conductance between MoS_2 and SiO_2 ($\text{TBC} \sim 15 \text{ MWm}^{-2}\text{K}^{-1}$).⁵⁰

We also compare the measurements with our simulations in Fig. 4b. The simulations including self-heating (solid lines) faithfully reproduce the experimental data, while simulations without self-heating (dashed lines) reach much higher current. The measured transconductance ($g_m = \partial I_D / \partial V_{GS}$) decreases with increasing gate voltage V_{GS} . In transistors based on typical bulk semiconductors (*e.g.* Si or III-Vs) such behavior is attributed to either contact resistance or mobility degradation from increased surface scattering at the higher transverse electric fields.^{27,51} However, $2R_C$ only accounts for $\sim 26\%$ of the total resistance even at $n = 2 \times 10^{13} \text{ cm}^{-2}$ for this MoS_2 device, and we find no degradation of mobility with increasing V_{GS} (Fig. 3a), as the electrons are already highly confined within the three-atom-thick semiconductor. The g_m decrease is also more pronounced at higher V_{DS} , *i.e.* higher input power, indicating that self-heating effects limit our MoS_2 transistor performance at high fields.

Simulations without self-heating (dashed lines in Fig. 4b) reveal this transistor could reach $I_{\text{on}} \approx 1.2 \text{ mA}/\mu\text{m}$ at $n \approx 2 \times 10^{13} \text{ cm}^{-2}$ and $V_{\text{DS}} = 5 \text{ V}$. These findings are consistent with recent studies of velocity saturation in monolayer MoS₂,^{43,52} underlining that self-heating dominates the measured high-field behavior, and suggesting that other reports of high current in 2D transistors are also limited by self-heating.^{16,18,53} (Also see Supporting Section S7.) We note that even with thinner insulating substrates (here the SiO₂ is only 30 nm), thermal dissipation is limited by poor heat transfer across the weak van der Waals MoS₂-SiO₂ interface, which is equivalent in thermal resistance to $\sim 90 \text{ nm}$ of SiO₂.⁵⁰ Thus, future efforts must consider improving heat dissipation in 2D transistors or operating them in a transient regime that is faster than typical thermal time constants,⁵² which are sub-nanosecond for the 2D material⁵⁴ and of the order 10-100 ns for the transistor including its gate and dielectrics.⁵⁵

Benchmarking: Figure 5a compares our results with other reports of high current in 2D semiconductors (from monolayer to $\sim 14 \text{ nm}$ thick) and various doping studies, including a fully-depleted Si nanowire FET.⁵⁶ Here we normalize the current by the conduction area [$J_{\text{on}} = I_{\text{on}}/(Wt_{\text{ch}})$], as opposed to only channel width to account for the channel thickness t_{ch} , which is a key limiter in transistor scaling.⁵⁷ Figure 5a reveals that while many 2D transistors display good on/off ratio, they lack the current density to compete with high-performance Si technology. By achieving high current drive in atomically thin, monolayer MoS₂ we surpass the current density of Si nanowires while maintaining good electrostatic control, highlighting the large current density and excellent electrostatics of 2D semiconductors.

These are the monolayer semiconductor transistors with the best current density reported to date, approaching IRDS low-power requirements⁹ both in terms of I_{on} and I_{off} . We also compare our results with other 2D material doping studies by plotting I_{on} vs. $I_{\text{on}}/I_{\text{off}}$ in Fig. 5b. As before, we emphasize that doping methods of 2D materials should not only be evaluated on the basis of R_{sh} , R_{C} , and I_{on} , but also on SS and $I_{\text{on}}/I_{\text{off}}$, as the inability to turn off 2D FETs could be an indication of charge traps. Figure 5b shows that most doping methods can induce high current in 2D semiconductors, but often by sacrificing $I_{\text{on}}/I_{\text{off}}$. As with our observations of trapping vs. doping using AlO_x, the doping methods that display low $I_{\text{on}}/I_{\text{off}}$ could be introducing a substantial number of mid-gap traps. Furthermore, many of these methods have not been applied to 2D monolayers (as in this work), which are electrostatically more favorable and represent the “ultimate atomic limit” of semiconductors.

Finally, in Fig. 5c we compare the I_{on} achieved in this work and previous studies of monolayer MoS₂ as a function of transistor channel length, at the same $V_{\text{DS}} = 1 \text{ V}$ and maximum V_{GS} reported. Solid curves represent a simple model with $I_{\text{D}} = V_{\text{DS}}/(LR_{\text{sh}} + 2R_{\text{C}})$ where $R_{\text{sh}} = (qn\mu)^{-1} \approx 8.1 \text{ k}\Omega/\square$ is

the average channel sheet resistance with $n = 2.2 \times 10^{13} \text{ cm}^{-2}$, $\mu = 35 \text{ cm}^2\text{V}^{-1}\text{s}^{-1}$, and $R_c = 1 \text{ k}\Omega \cdot \mu\text{m}$ (achieved previously,^{5,43} gray line) or $480 \text{ }\Omega \cdot \mu\text{m}$ (achieved in this work, black line). The horizontal red lines show the IRDS low-power (LP) and high-performance (HP) requirements (at a more aggressive 0.75 V in 10-20 nm gate length FETs).⁹ It is evident that micron-scale devices are limited by their mobility, but short channels ($L < 2R_c/R_{\text{sh}}$, especially $< 100 \text{ nm}$) are strongly limited by their contacts. Thus, we expect that the largest improvements of short-channel MoS₂ transistors will be achieved by further reducing the contact resistance, together with reduction of equivalent oxide thickness (EOT) which will allow lowering V_{GS} . Other benchmarking data on multi-layer and other 2D semiconductor transistors are summarized on a new website⁵⁸ recently launched while preparing this manuscript.

CONCLUSIONS

We have demonstrated the doping effect of sub-stoichiometric AlO_x on monolayer CVD-grown MoS₂. By activating dopants and reducing trap densities, we achieved record transistor current of nearly 700 $\mu\text{A}/\mu\text{m}$ at 5 V ($\sim 300 \text{ }\mu\text{A}/\mu\text{m}$ at 1 V), limited primarily by self-heating due to large current densities. The doping achieved with AlO_x is stable, also yielding excellent sheet resistance (down to 7 $\text{k}\Omega/\square$) and contact resistance (down to $480 \text{ }\Omega \cdot \mu\text{m}$) for monolayer MoS₂ without degrading mobility or subthreshold swing. In contrast, previous 2D material doping methods often induced large density of interface traps that limit on- and off-state current. These interface traps can also lead to an overestimation of carrier density and underestimation of mobility. Future work should focus on selective doping near contacts, doping of the channel for threshold voltage control, *p*-type doping to enable CMOS and reducing the gate oxide thickness for lower gate voltages of high-performance transistors and 2D circuits.

METHODS

MoS₂ FET Fabrication: Monolayer MoS₂ was deposited using a chemical vapor deposition (CVD)²⁰ process directly onto $t_{\text{ox}} = 30 \text{ nm}$ of thermal dry SiO₂ on p^{++} Si substrate (electrical resistivity of 1 to 5 $\text{m}\Omega \cdot \text{cm}$), which acts as a global back-gate. The MoS₂ was first etched into $\sim 2 \text{ }\mu\text{m}$ wide rectangular channels using electron beam lithography (EBL) and a XeF₂ etch. Source and drain electrical contacts were defined using EBL with channel lengths varying between 180 nm and 3 μm . Pure Au contacts of 35 nm thickness were deposited on the MoS₂ using electron beam evaporation at high-vacuum ($\sim 8 \times 10^{-8}$ Torr) followed by lift-off in acetone and isopropyl alcohol cleaning.²¹ We stress the importance of using pure Au contacts to MoS₂ for a clean contact interface, compared to metals that oxidize or react

with the monolayer MoS₂. Fabricating Au contacts without Ti or Cr adhesion layers requires careful processing, applying very little agitation to the sample during lift-off, and utilizing the pure Au only for the contacts and leads, not the large probing pads (which do have a ~3 nm Ti adhesion layer). The large probing pads (away from the device channels) were a stack of 20 nm SiO₂, 3 nm Ti and 40 nm Au, with the additional SiO₂ to limit leakage current from the 200 × 200 μm pad area to the substrate. If these steps are carefully followed, our liftoff yield is about 70% for the Au contacts vs. the Ti/Au probing pads.

Measurements: All electrical measurements in this work were performed in the dark and under vacuum (<10⁻⁵ Torr) using a Keithley 4200-SCS parameter analyzer, in a Janis ST-100 probe station, at room temperature. We scratched through the AlO_x layer on top of the electrical pads using the W probe tip to make electrical contact with the Au. All plotted *I-V* data shows both forward and backward sweeps, indicating minimal hysteresis in our devices. For measuring the transistor on/off current ratio, we divide the maximum on current (*I*_{on}) by the minimum off current (*I*_{off}) over the whole gate voltage sweep. Raman and PL data were taken using a Horiba Labram with 532 nm excitation laser.

AlO_x Deposition: For the AlO_x capping and doping layer, an Al seed layer was first deposited on the MoS₂ devices by electron beam evaporation at a base pressure of ~4 × 10⁻⁷ Torr. After exposure to air, the Al seed layer immediately oxidizes into AlO_x. Supporting Section S8 shows the Al seed layer doping effect on MoS₂ FETs by applying several cycles of 1.5 nm Al deposition and oxidizing in air for 2 hours. We use a 1 nm Al layer to seed ~15 nm of AlO_x deposited by ALD at 150°C with a trimethylaluminum precursor and H₂O oxidizing step. The Al seed layer promotes the nucleation of ALD AlO_x for complete coverage of the MoS₂.⁵⁹ We also found that hydrogen annealing can effectively reduce the AlO_x, increasing the trap density and doping (Supporting Section S9).

ASSOCIATED CONTENT

Supporting Information: Available free of charge at <https://pubs.acs.org/doi/xx.xx/acs.nano.xxx>.

Raman data of MoS₂ capped by AlO_x without Al seed layer; modeling subthreshold swing (SS), charge trapping and doping; top-gate transistor measurements; transfer length method (TLM) measurements for contact and sheet resistance; transistor model with and without self-heating; effect of Al seed layer thickness on AlO_x doping; effect of H₂ anneals.

REFERENCES

- 1 Auth, C., Aliyarukunju, A., Asoro, M., Bergstrom, D., Bhagwat, V., Birdsall, J., Bisnik, N., Buehler, M., Chikarmane, V. & Ding, G.A 10 nm High Performance and Low-Power CMOS Technology Featuring 3rd Generation FinFET Transistors, Self-Aligned Quad Patterning, Contact over Active Gate and Cobalt Local Interconnects. *IEEE International Electron Devices Meeting*. **2017** 29.21.21-29.21.24.
- 2 Bae, G., Bae, D.-I., Kang, M., Hwang, S., Kim, S., Seo, B., Kwon, T., Lee, T., Moon, C. & Choi, Y. 3nm GAA Technology Featuring Multi-Bridge-Channel FET for Low Power and High Performance Applications. *IEEE International Electron Devices Meeting*. **2018** 28.27.21-28.27.24.
- 3 Murmann, B., Nikaeen, P., Connelly, D. J. & Dutton, R. W., Impact of Scaling on Analog Performance and Associated Modeling Needs. *IEEE Transactions on Electron Devices* **2006**, 53 (9), 2160-2167.
- 4 Fiori, G., Bonaccorso, F., Iannaccone, G., Palacios, T., Neumaier, D., Seabaugh, A., Banerjee, S. K. & Colombo, L., Electronics Based on Two-Dimensional Materials. *Nature Nanotechnology* **2014**, 9 (10), 768.
- 5 English, C. D., Smithe, K. K., Xu, R. L. & Pop, E. Approaching Ballistic Transport in Monolayer MoS₂ Transistors with Self-Aligned 10 nm Top Gates. *IEEE International Electron Devices Meeting*. **2016** 5.6. 1-5.6. 4.
- 6 Baugher, B. W. H., Churchill, H. O. H., Yang, Y. & Jarillo-Herrero, P., Optoelectronic Devices Based on Electrically Tunable P-N Diodes in a Monolayer Dichalcogenide. *Nature Nanotechnology* **2014**, 9 (4), 262 – 267.
- 7 Wang, C.-H., McClellan, C., Shi, Y., Zheng, X., Chen, V., Lanza, M., Pop, E. & Wong, H.-S. P. 3d Monolithic Stacked 1T1R Cells Using Monolayer MoS₂ FET and hBN RRAM Fabricated at Low (150° C) Temperature. *IEEE International Electron Devices Meeting*. **2018** 22.25. 21-22.25. 24.
- 8 Choi, M., Park, Y. J., Sharma, B. K., Bae, S.-R., Kim, S. Y. & Ahn, J.-H., Flexible Active-Matrix Organic Light-Emitting Diode Display Enabled by MoS₂ Thin-Film Transistor. *Science Advances* **2018**, 4 (4), eaas8721.
- 9 2020 International Roadmap for Devices and Systems. <https://irds.ieee.org/>.
- 10 Zhao, P. D., Kiriya, D., Azcatl, A., Zhang, C. X., Tosun, M., Liu, Y. S., Hettick, M., Kang, J. S., McDonnell, S., Santosh, K. C., Guo, J. H., Cho, K., Wallace, R. M. & Javey, A., Air Stable P-Doping of WSe₂ by Covalent Functionalization. *ACS Nano* **2014**, 8 (10), 10808-10814.
- 11 Yu, L. L., Zubair, A., Santos, E. J. G., Zhang, X., Lin, Y. X., Zhang, Y. H. & Palacios, T., High-Performance WSe₂ Complementary Metal Oxide Semiconductor Technology and Integrated Circuits. *Nano Lett.* **2015**, 15 (8), 4928-4934.
- 12 Fang, H., Tosun, M., Seol, G., Chang, T. C., Takei, K., Guo, J. & Javey, A., Degenerate N-Doping of Few-Layer Transition Metal Dichalcogenides by Potassium. *Nano Lett.* **2013**, 13 (5), 1991-1995.
- 13 Kiriya, D., Tosun, M., Zhao, P. D., Kang, J. S. & Javey, A., Air-Stable Surface Charge Transfer Doping of MoS₂ by Benzyl Viologen. *J. Am. Chem. Soc.* **2014**, 136 (22), 7853-7856.
- 14 Fathipour, S., Pandey, P., Fullerton-Shirey, S. & Seabaugh, A., Electric-Double-Layer Doping of WSe₂ Field-Effect Transistors Using Polyethylene-Oxide Cesium Perchlorate. *Journal of Applied Physics* **2016**, 120 (23), 234902.
- 15 Cai, L., McClellan, C. J., Koh, A. L., Li, H., Yalon, E., Pop, E. & Zheng, X., Rapid Flame Synthesis of Atomically Thin MoO₃ Down to Monolayer Thickness for Effective Hole Doping of WSe₂. *Nano Lett.* **2017**, 17 (6), 3854-3861.
- 16 Rai, A., Valsaraj, A., Movva, H. C. P., Roy, A., Ghosh, R., Sonde, S., Kang, S. W., Chang, J. W., Trivedi, T., Dey, R., Guchhait, S., Larentis, S., Register, L. F., Tutuc, E. & Banerjee, S. K., Air Stable Doping and Intrinsic Mobility Enhancement in Monolayer Molybdenum Disulfide by Amorphous Titanium Suboxide Encapsulation. *Nano Lett.* **2015**, 15 (7), 4329-4336.

- 17 Leonhardt, A., Chiappe, D., Afanas'ev, V. V., El Kazzi, S., Shlyakhov, I., Conard, T., Franquet, A., Huyghebaert, C. & De Gendt, S., Material-Selective Doping of 2D TMDC through Al_xO_y Encapsulation. *ACS Applied Materials & Interfaces* **2019**, *11* (45), 42697-42707.
- 18 Yang, L. M., Majumdar, K., Liu, H., Du, Y. C., Wu, H., Hatzistergos, M., Hung, P. Y., Tieckelmann, R., Tsai, W., Hobbs, C. & Ye, P. D., Chloride Molecular Doping Technique on 2D Materials: WS_2 and MoS_2 . *Nano Lett.* **2014**, *14* (11), 6275-6280.
- 19 Grenouillet, L., Vinet, M., Gimbert, J., Giraud, B., Noel, J., Liu, Q., Khare, P., Jaud, M., Le Tiec, Y. & Wacquez, R. UTBB FDSOI Transistors with Dual STI for a Multi- V_t Strategy at 20nm Node and Below. *IEEE International Electron Devices Meeting*. **2012** 3.6. 1-3.6. 4.
- 20 Smithe, K. K. H., Suryavanshi, S. V., Rojo, M. M., Tedjarati, A. D. & Pop, E., Low Variability in Synthetic Monolayer MoS_2 Devices. *ACS Nano* **2017**, *11* (8), 8456-8463.
- 21 English, C. D., Shine, G., Dorgan, V. E., Saraswat, K. C. & Pop, E., Improved Contacts to MoS_2 Transistors by Ultra-High Vacuum Metal Deposition. *Nano Lett.* **2016**, *16* (6), 3824-3830.
- 22 Song, S. M. & Cho, B. J., Contact Resistance in Graphene Channel Transistors. *Carbon Letters* **2013**, *14* (3), 162-170.
- 23 Fleetwood, D. M. & Senior, M., "Border Traps" in MOS Devices. *IEEE Transactions on Nuclear Science* **1992**, *39* (2), 269-271.
- 24 Fleetwood, D. M., Winokur, P. S., Reber, R. A., Meisenheimer, T. L., Schwank, J. R., Shaneyfelt, M. R. & Riewe, L. C., Effects of Oxide Traps, Interface Traps, and "Border Traps" on Metal-Oxide-Semiconductor Devices. *Journal of Applied Physics* **1993**, *73* (10), 5058-5074.
- 25 Nguyen, L. D., Larson, L. E. & Mishra, U. K., Ultra-High-Speed Modulation-Doped Field-Effect Transistors - a Tutorial Review. *Proc. IEEE* **1992**, *80* (4), 494-518.
- 26 Kirsch, P. D., Sivasubramani, P., Huang, J., Young, C., Quevedo-Lopez, M., Wen, H., Alshareef, H., Choi, K., Park, C. & Freeman, K., Dipole Model Explaining High-K/Metal Gate Field Effect Transistor Threshold Voltage Tuning. *Applied Physics Letters* **2008**, *92* (9), 092901.
- 27 Streetman, B. & Banerjee, S. *Solid State Electronic Devices*. 6 edn, 311 (Prentice Hall, 2005).
- 28 Xiong, K. & Robertson, J., Oxygen Vacancies in High Dielectric Constant Oxides La_2O_3 , Lu_2O_3 , and LaLuO_3 . *Applied Physics Letters* **2009**, *95* (2), 022903.
- 29 Foster, A. S., Gejo, F. L., Shluger, A. & Nieminen, R. M., Vacancy and Interstitial Defects in Hafnia. *Physical Review B* **2002**, *65* (17), 174117.
- 30 Dicks, O. A., Cottom, J., Shluger, A. L. & Afanas'ev, V. V., The Origin of Negative Charging in Amorphous Al_2O_3 Films: The Role of Native Defects. *Nanotechnology* **2019**, *30* (20), 205201.
- 31 Ghatak, S., Pal, A. N. & Ghosh, A., Nature of Electronic States in Atomically Thin MoS_2 Field-Effect Transistors. *ACS Nano* **2011**, *5* (10), 7707-7712.
- 32 Jena, D. in *Polarization Effects in Semiconductors*, pp. 161-216 (Springer, 2008).
- 33 Lee, Y., Fiore, S. & Luisier, M. Ab Initio Mobility of Single-Layer MoS_2 and WS_2 : Comparison to Experiments and Impact on the Device Characteristics. *IEEE International Electron Devices Meeting*. **2019** 24.24. 21-24.24. 24.
- 34 Suryavanshi, S. V. & Pop, E., S2ds: Physics-Based Compact Model for Circuit Simulation of Two-Dimensional Semiconductor Devices Including Non-Idealities. *Journal of Applied Physics* **2016**, *120* (22), 224503.
- 35 Jeon, T. S., White, J. M. & Kwong, D. L., Thermal Stability of Ultrathin ZrO_2 Films Prepared by Chemical Vapor Deposition on Si(100). *Applied Physics Letters* **2001**, *78* (3), 368-370.
- 36 Guha, S., Gusev, E. P., Okorn-Schmidt, H., Copel, M., Ragnarsson, L.-Å., Bojarczuk, N. A. & Ronsheim, P., High Temperature Stability of Al_2O_3 Dielectrics on Si: Interfacial Metal Diffusion and Mobility Degradation. *Applied Physics Letters* **2002**, *81* (16), 2956-2958.
- 37 Vaziri, S., Chen, V., Cai, L., Jiang, Y., Chen, M. E., Grady, R. W., Zheng, X. & Pop, E., Ultrahigh Doping of Graphene Using Flame-Deposited MoO_3 . *IEEE Electron Device Letters* **2020**, *41* (10), 1592-1595.

- 38 Schauble, K., Zakhidov, D., Yalon, E., Deshmukh, S., Grady, R. W., Cooley, K. A., McClellan, C. J., Vaziri, S., Passarello, D. & Mohny, S. E., Uncovering the Effects of Metal Contacts on Monolayer MoS₂. *ACS Nano* **2020**, *14* (11), 14798–14808.
- 39 Wu, C.-L., Yuan, H., Li, Y., Gong, Y., Hwang, H. Y. & Cui, Y., Gate-Induced Metal–Insulator Transition in MoS₂ by Solid Superionic Conductor LaF₃. *Nano Lett.* **2018**, *18* (4), 2387-2392.
- 40 Allain, A., Kang, J. H., Banerjee, K. & Kis, A., Electrical Contacts to Two-Dimensional Semiconductors. *Nat. Mater.* **2015**, *14* (12), 1195-1205.
- 41 Arutchelvan, G., de la Rosa, C. J. L., Matagne, P., Sutar, S., Radu, I., Huyghebaert, C., De Gendt, S. & Heyns, M., From the Metal to the Channel: A Study of Carrier Injection through the Metal/2D Mos 2 Interface. *Nanoscale* **2017**, *9* (30), 10869-10879.
- 42 Szabó, Á., Jain, A., Parzefall, M., Novotny, L. & Luisier, M., Electron Transport through Metal/MoS₂ Interfaces: Edge-or Area-Dependent Process? *Nano Lett.* **2019**, *19* (6), 3641-3647.
- 43 Smithe, K. K., English, C. D., Suryavanshi, S. V. & Pop, E., High-Field Transport and Velocity Saturation in Synthetic Monolayer MoS₂. *Nano Lett.* **2018**, *18* (7), 4516-4522.
- 44 Frindt, R. F., Single Crystals of MoS₂ Several Molecular Layers Thick. *Journal of Applied Physics* **1966**, *37* (4), 1928-1929.
- 45 Yu, J., Liu, G., Sumant, A. V., Goyal, V. & Balandin, A. A., Graphene-on-Diamond Devices with Increased Current-Carrying Capacity: Carbon Sp²-on-Sp³ Technology. *Nano Lett.* **2012**, *12* (3), 1603-1608.
- 46 Chen, Y.-F. & Fuhrer, M., Electric-Field-Dependent Charge-Carrier Velocity in Semiconducting Carbon Nanotubes. *Physical Review Letters* **2005**, *95* (23), 236803.
- 47 Khater, M. H., Zhang, Z., Cai, J., Lavoie, C., D'Emic, C., Yang, Q., Yang, B., Guillorn, M., Klaus, D. & Ott, J. A., High-K Metal-Gate Fully Depleted SOI CMOS with Single-Silicide Schottky Source/Drain with Sub-30-nm Gate Length. *IEEE Electron Device Letters* **2010**, *31* (4), 275-277.
- 48 Zota, C. B., Lindelow, F., Wernersson, L. & Lind, E. Ingaas Nanowire Mosfets with I_{on} = 555 uA/um at I_{off} = 100 nA/um and V_{dd} = 0.5 V. *Symp. VLSI Technol. Dig. Tech.* **2016**.
- 49 Rakheja, S., Lundstrom, M. S. & Antoniadis, D. A., An Improved Virtual-Source-Based Transport Model for Quasi-Ballistic Transistors—Part I: Capturing Effects of Carrier Degeneracy, Drain-Bias Dependence of Gate Capacitance, and Nonlinear Channel-Access Resistance. *IEEE Transactions on Electron Devices* **2015**, *62* (9), 2786-2793.
- 50 Yalon, E., Aslan, Ö. B., Smithe, K. K. H., McClellan, C. J., Suryavanshi, S. V., Xiong, F., Sood, A., Neumann, C. M., Xu, X., Goodson, K. E., Heinz, T. F. & Pop, E., Temperature Dependent Thermal Boundary Conductance of Monolayer MoS₂ by Raman Thermometry. *ACS Applied Materials & Interfaces* **2017**, *9* (49), 43013-43020.
- 51 Taur, Y. & Ning, T. H. *Fundamentals of Modern Vlsi Devices*. (Cambridge university press, 2013).
- 52 Nathawat, J., Smithe, K., English, C., Yin, S., Dixit, R., Randle, M., Arabchigavkani, N., Barut, B., He, K., Pop, E. & Bird, J., Transient Hot-Carrier Dynamics and Intrinsic Velocity Saturation in Monolayer MoS₂. *Physical Review Materials* **2020**, *4* (1), 014002.
- 53 Liu, Y., Jian, G., Ye-Cun, W., Enbo, Z., O., W. N., Qiyuan, H., Hao, W., Hung-Chieh, C., Yang, X., Imran, S., Yu, H. & Xiangfeng, D., Pushing the Performance Limit of Sub-100 nm Molybdenum Disulfide Transistors. *Nano Lett.* **2016**, *16* (10), 6337-6342.
- 54 Suryavanshi, S. V., Gabourie, A. J., Barati Farimani, A. & Pop, E., Thermal Boundary Conductance of Two-Dimensional MoS₂ Interfaces. *Journal of Applied Physics* **2019**, *126* (5), 055107.
- 55 Islam, S., Li, Z., Dorgan, V. E., Bae, M.-H. & Pop, E., Role of Joule Heating on Current Saturation and Transient Behavior of Graphene Transistors. *IEEE Electron Device Letters* **2013**, *34* (2), 166-168.
- 56 Singh, N., Agarwal, A., Bera, L. K., Liow, T. Y., Yang, R., Rustagi, S. C., Tung, C. H., Kumar, R., Lo, G. Q., Balasubramanian, N. & Kwong, D. L., High-Performance Fully Depleted Silicon-Nanowire (Diameter ≤ 5 nm) Gate-All-around CMOS Devices. *IEEE Electron Device Letters* **2006**, *27* (5), 383-386.

- 57 Frank, D. J., Dennard, R. H., Nowak, E., Solomon, P. M., Taur, Y. & Wong, H. S. P., Device Scaling Limits of Si Mosfets and Their Application Dependencies. *Proc. IEEE* **2001**, 89 (3), 259-288.
- 58 McClellan, C. J., Suryavanshi, S. V., English, C. D., Smithe, K. K. H., Bailey, C. S., Grady, R. W. & Pop, E. *2D Device Trends*, <<http://2d.stanford.edu>> (Accessed on: 10/20/2020).
- 59 Kim, S., Junghyo, N., Insun, J., Davood, S., Luigi, C., Zhen, Y., Emanuel, T. & K, B. S., Realization of a High Mobility Dual-Gated Graphene Field-Effect Transistor with Al₂O₃ Dielectric. *Applied Physics Letters* **2009**, 94 (6), 062107.
- 60 Chandrasekhar, M., Renucci, J. & Cardona, M., Effects of Interband Excitations on Raman Phonons in Heavily Doped N-Si. *Physical Review B* **1978**, 17 (4), 1623.
- 61 Tsang, J., Freitag, M., Perebeinos, V., Liu, J. & Avouris, P., Doping and Phonon Renormalization in Carbon Nanotubes. *Nature Nanotech.* **2007**, 2 (11), 725-730.
- 62 Chakraborty, B., Bera, A., Muthu, D., Bhowmick, S., Waghmare, U. V. & Sood, A. K., Symmetry-Dependent Phonon Renormalization in Monolayer MoS₂ Transistor. *Physical Review B* **2012**, 85 (16), 161403.
- 63 Yalon, E., McClellan, C. J., Smithe, K. K., Muñoz Rojo, M., Xu, R. L., Suryavanshi, S. V., Gabourie, A. J., Neumann, C. M., Xiong, F. & Farimani, A. B., Energy Dissipation in Monolayer MoS₂ Electronics. *Nano Lett.* **2017**, 17 (6), 3429-2433.
- 64 Sanne, A., Rudresh, G., Amrithesh, R., Nagavalli, Y. M., Heon, S. S., Ankit, S., Karalee, J., Leo, M., Rajesh, R., Deji, A. & Sanjay, B., Radio Frequency Transistors and Circuits Based on CVD MoS₂ FETs. *Nano Lett.* **2015**, 15 (8), 5039-5045.
- 65 Li, L., Engel, M., Farmer, D. B., Han, S.-j. & Wong, H.-S. P., High-Performance P-Type Black Phosphorus Transistor with Scandium Contact. *ACS Nano* **2016**, 10 (6), 4672-4677.
- 66 Yang, L., Qiu, G., Si, M., Charnas, A., Milligan, C., Zemlyanov, D., Zhou, H., Du, Y., Lin, Y. & Tsai, W. Few-Layer Black Phosphorous PMOSFETs with BN/Al₂O₃ Bilayer Gate Dielectric: Achieving I_{on}=850 μA/μm, G_m=340 μS/μm, and R_c=0.58 kΩ·μm. *IEEE International Electron Devices Meeting*. **2016** 5.5. 1-5.5. 4.
- 67 Yang, L., Lee, R., Rao, S. P., Tsai, W. & Ye, P. 10 nm Nominal Channel Length MoS₂ FETs with EOT 2.5 nm and 0.52 mA/μm Drain Current. *Device Research Conference (DRC), 2015 73rd Annual*. **2015** 237-238.
- 68 Chou, A.-S., Shen, P.-C., Cheng, C.-C., Lu, L.-S., Chueh, W.-C., Li, M.-Y., Pitner, G., Chang, W.-H., Wu, C.-I., Kong, J., Li, L.-J. & Wong, H.-S. P. High on-Current 2D Nfet of 390 uA/um at V_{ds} = 1V Using Monolayer CVD MoS₂ without Intentional Doping. *2020 IEEE Symposium on VLSI Technology*. **2020**.
- 69 Tosun, M., Chan, L., Amani, M., Roy, T., Ahn, G. H., Taheri, P., Carraro, C., Ager, J. W., Maboudian, R. & Javey, A., Air-Stable N-Doping of WSe₂ by Anion Vacancy Formation with Mild Plasma Treatment. *ACS Nano* **2016**, 10 (7), 6853-6860.
- 70 Yamamoto, M., Shu, N., Keiji, U. & Kazuhito, T., Self-Limiting Oxides on WSe₂ as Controlled Surface Acceptors and Low-Resistance Hole Contacts. *Nano Lett.* **2016**, 16 (4), 2720-2727.
- 71 Liu, B., Ma, Y., Zhang, A., Chen, L., Abbas, A. N., Liu, Y., Shen, C., Wan, H. & Zhou, C., High-Performance WSe₂ Field-Effect Transistors Via Controlled Formation of in-Plane Heterojunctions. *ACS Nano* **2016**, 10 (5), 5153-5160.
- 72 De la Rosa, C. J. L., Nourbakhsh, A., Heyne, M., Asselberghs, I., Huyghebaert, C., Radu, I., Heyns, M. & De Gendt, S., Highly Efficient and Stable MoS₂ FETs with Reversible N-Doping Using a Dehydrated Poly(Vinyl-Alcohol) Coating. *Nanoscale* **2016**, 9 (1), 258-265.
- 73 Cao, W., Liu, W., Kang, J. & Banerjee, K., An Ultra-Short Channel Monolayer MoS₂ FET Defined by the Curvature of a Thin Nanowire. *IEEE Electron Device Letters* **2016**, 37 (11), 1497-1500.
- 74 Nourbakhsh, A., Zubair, A., Sajjad, R. N., Tavakkoli KG, A., Chen, W., Fang, S., Ling, X., Kong, J., Dresselhaus, M. S. & Kaxiras, E., MoS₂ Field-Effect Transistor with Sub-10 nm Channel Length. *Nano Lett.* **2016**, 16 (12), 7798-7806.
- 75 Lembke, D. & Kis, A., Breakdown of High-Performance Monolayer MoS₂ Transistors. *ACS Nano* **2012**, 6 (11), 10070-10075.

- 76 Smithe, K. K., English, C. D., Suryavanshi, S. V. & Pop, E., Intrinsic Electrical Transport and Performance Projections of Synthetic Monolayer MoS₂ Devices. *2D Materials* **2017**, 4 (1), 011009.
- 77 Yu, Z., Zhu, Y., Li, W., Shi, Y., Zhang, G., Chai, Y. & Wang, X. Toward High-Mobility and Low-Power 2D MoS₂ Field-Effect Transistors. *IEEE International Electron Devices Meeting*. **2018** 22.24. 21-22.24. 24.
- 78 Patel, K. A., Grady, R. W., Smithe, K. K., Pop, E. & Sordan, R., Ultra-Scaled MoS₂ Transistors and Circuits Fabricated without Nanolithography. *2D Materials* **2019**, 7 (1), 015018.

AUTHOR INFORMATION

Corresponding Author: *E-mail epop@stanford.edu

Author Contributions: C.J.M., E.Y. and E.P. conceived the experiments and wrote the manuscript with input from all authors. K.K.H.S. grew the MoS₂. C.J.M., S.S., and E.P. developed the subthreshold and drift current models. C.J.M. fabricated the devices. C.J.M. and E.Y. performed electrical, PL, and Raman characterizations.

Competing interests: The authors declare that they have no competing interests.

ACKNOWLEDGMENTS

Fabrication and measurements were performed in part at the Stanford Nanofabrication Facility (SNF) and the Stanford Nano Shared Facilities (SNSF), which received funding from the National Science Foundation (NSF) as part of National Nanotechnology Coordinated Infrastructure Award ECCS-1542152. This work was supported in part by ASCENT, one of six centers in JUMP, a Semiconductor Research Corporation (SRC) program sponsored by DARPA, and the Stanford SystemX Alliance. C.J.M. acknowledged support from the NSF Graduate Research Fellowship. K.K.H.S. acknowledged partial support from the Stanford Graduate Fellowship (SGF) program and NSF Graduate Research Fellowship under grant no. DGE-114747.

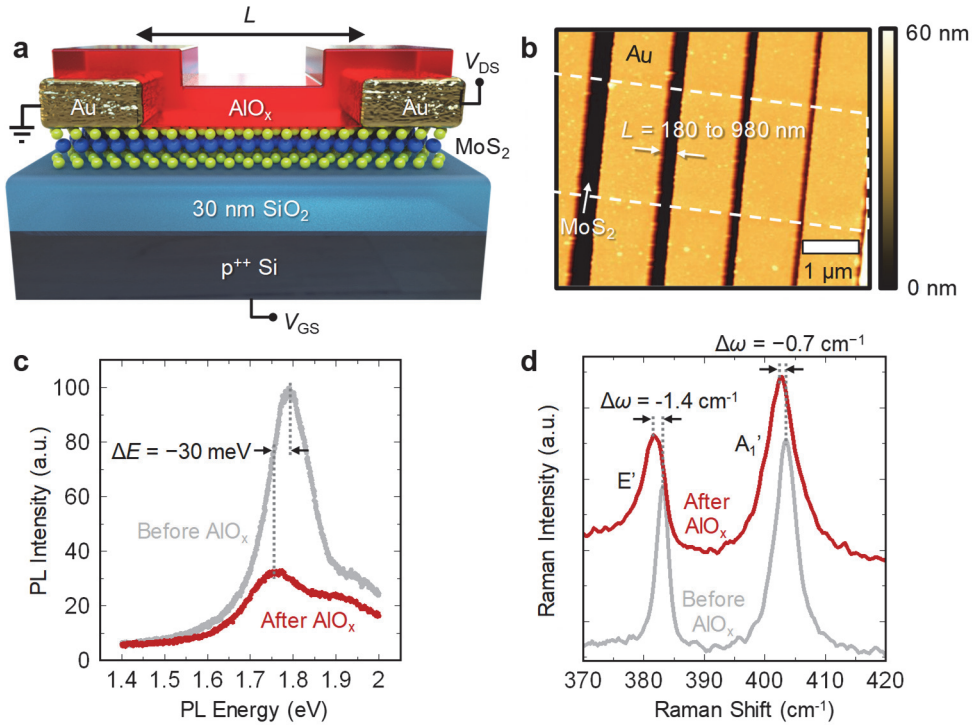


Fig. 1. AlO_x doped MoS_2 FET. (a) Schematic of FET with Au contacts, 16 nm AlO_x capping, and monolayer MoS_2 channel grown on $t_{\text{ox}} = 30$ nm SiO_2 with a p^{++} Si substrate as a back-gate. (b) Atomic force microscopy (AFM) image of transfer length method (TLM) structures used for extracting contact and sheet resistances. (c) Photoluminescence (PL) measurements of MoS_2 before and after AlO_x deposition and N_2 annealing, showing a decrease of intensity and slight red-shift in PL peak position after AlO_x deposition. (d) Raman spectra of MoS_2 before and after AlO_x deposition. The AlO_x deposition induces a red-shift and asymmetry of the E' mode, consistent with the Fano effect of high doping,^{60,61} while the red-shift and peak broadening of the A_1' mode has also been correlated with MoS_2 doping.⁶² The corresponding full-width half-maximums (FWHM) before AlO_x are 3.2 cm^{-1} (6.1 cm^{-1}) for E' (A_1') which then increase after AlO_x deposition to 6.8 cm^{-1} (7.3 cm^{-1}) for E' (A_1').

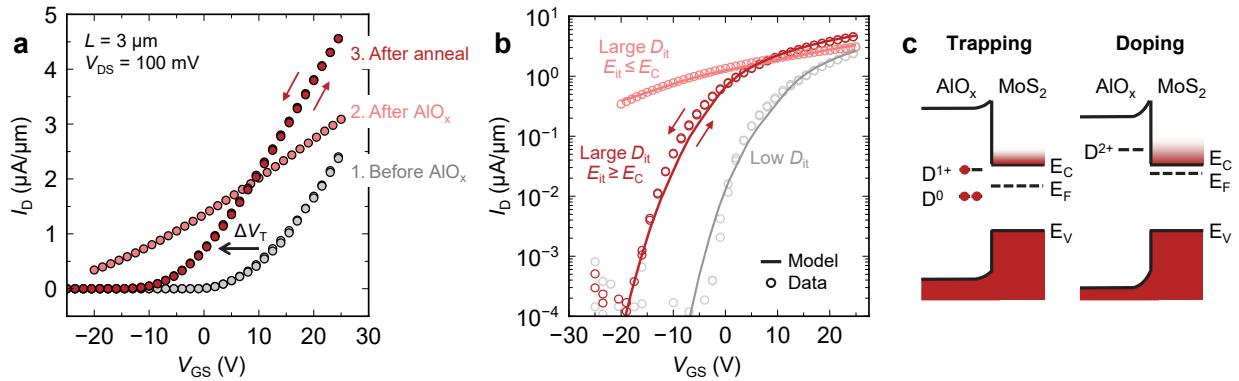


Fig. 2. Trapping and doping in MoS₂ FET. (a) Linear and (b) log scale measured transfer characteristics of MoS₂ FET before AlO_x deposition (gray), after AlO_x deposition (light red) and after 200°C N₂ anneal for 40 minutes (dark red). The -12 V shift in V_T after N₂ annealing indicates an induced negative charge density of $\sim 8.6 \times 10^{12} \text{ cm}^{-2}$ in the MoS₂. Interface trap model fitting shown in (b) matches the experimental data, demonstrating how mid-gap trap states can pin the MoS₂ Fermi level and reduce gate control. Small arrows show both backward and forward measurements (dual sweep), revealing minimal hysteresis. (c) Schematic band diagram of the trapping and doping states of the AlO_x/MoS₂ interface, D⁰ being a defect with no charge, D¹⁺ a defect with 1 positive charge, and D²⁺ a defect with 2 positive charges. Band bending in the AlO_x is shown schematically to illustrate presence of charge.

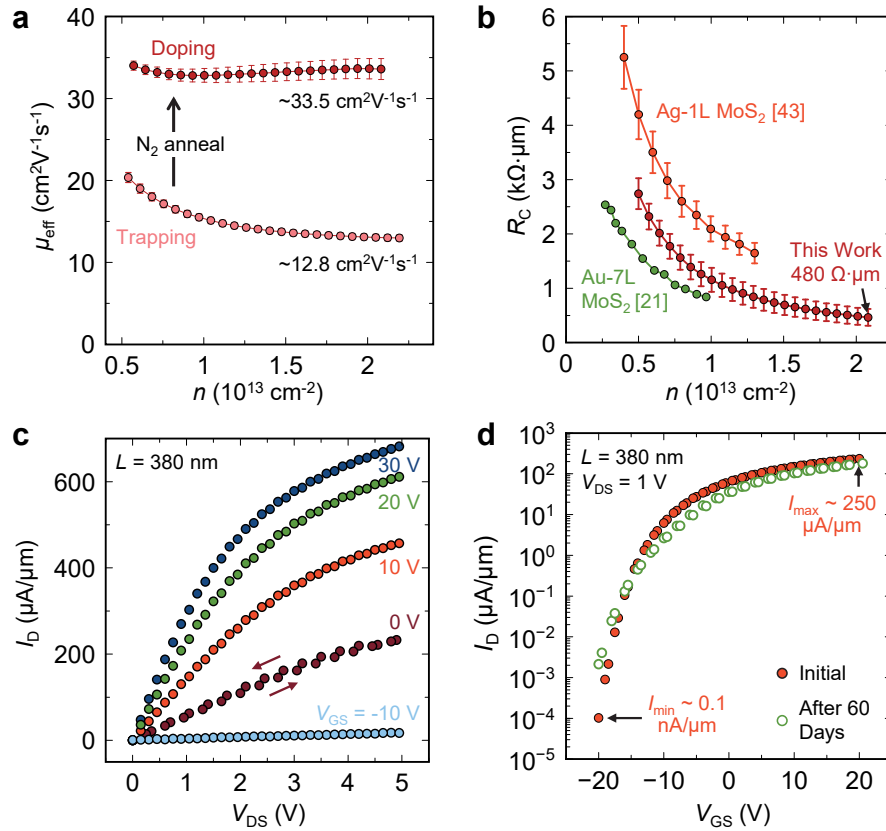


Fig. 3. Electrical characteristics in trapping and doping states of MoS₂ FET. (a) Effective mobility (μ_{eff}) and (b) contact resistance (R_C) extractions vs. electron concentration with the TLM. The doping state (dark red) demonstrates higher μ_{eff} than the trapping state (light red), as the reduction in traps yields a lower sheet resistance of the MoS₂. By reaching higher carrier density, our highly doped Au-1L MoS₂ FETs demonstrates lower R_C than previously measured R_C between Ag-1L MoS₂ and Au-7L MoS₂.^{21,43} (c) Measured output and (d) log-scale transfer characteristics of a 380 nm long AlO_x doped MoS₂ device, reaching nearly $\sim 700 \mu\text{A}/\mu\text{m}$ while maintaining a high on/off ratio of $\sim 10^6$. The doping method is stable with only slight degradation after 60 days in air, as shown in (d). Every I - V shows forward and backward measurements (small arrows), with minimal hysteresis.

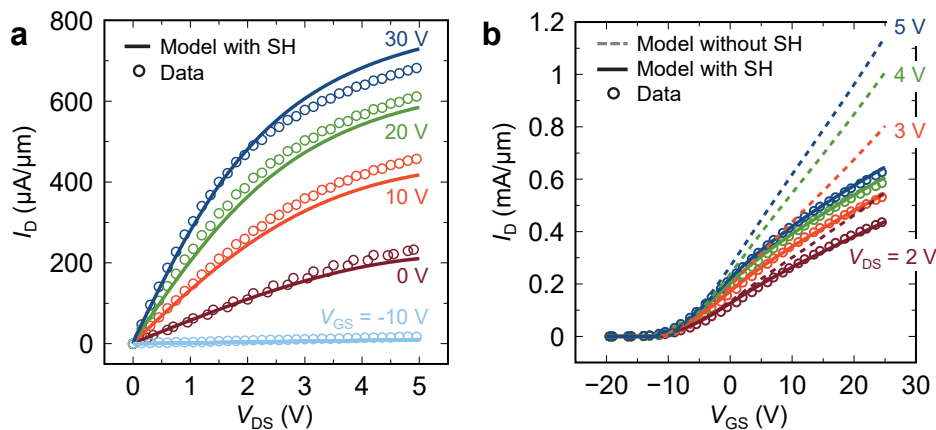


Fig. 4. High current density and self-heating in AlO_x -doped MoS_2 FET. Measured data (symbols) compared to model with self-heating (with SH, lines) and model without self-heating (without SH, dashed). The (a) output and (b) transfer characteristics correspond to the device in Figure 3, with $L = 380$ nm. The model includes self-heating with measured thermal conductance.⁶³ Including self-heating accurately reflects the saturation of current, while the model without self-heating suggests I_D could reach over $1 \text{ mA}/\mu\text{m}$. The simulations also capture the decrease of the saturation voltage (V_{Dsat}) with increasing V_{GS} , which is only modeled correctly when including self-heating.

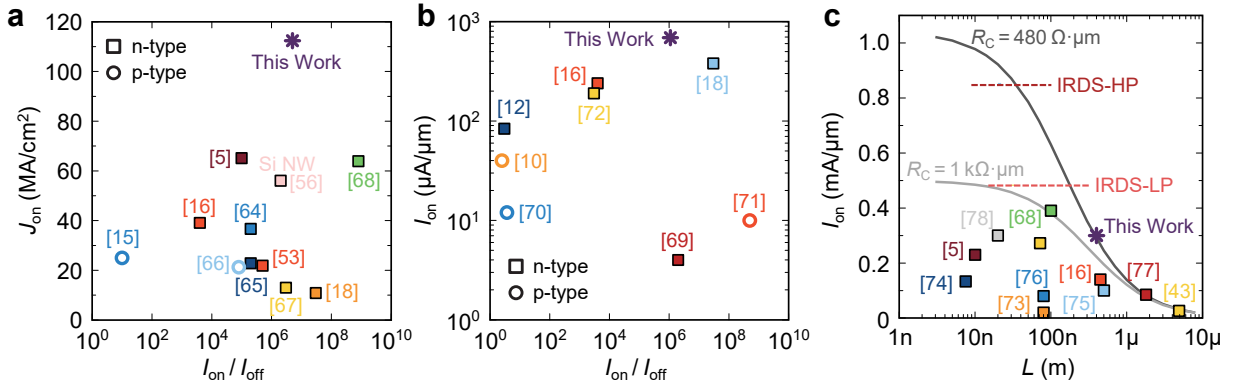


Fig. 5. Benchmarking various 2D semiconductor transistors. (a) Maximum current density ($J_{on} = I_{on}/t_{ch}$) vs. I_{on}/I_{off} for our monolayer MoS₂, for other high current 2D semiconductor devices^{5,15,16,18,53,64-68} of varying layer thickness ($0.6 \text{ nm} \leq t_{ch} \leq 14 \text{ nm}$), and a Si nanowire device.⁵⁶ (b) Maximum I_{on} vs. I_{on}/I_{off} of our AlO_x-doped MoS₂ compared with other doped 2D-FETs.^{10,12,16,18,69-72} While some doping methods yield high I_{on} , the I_{on}/I_{off} can be much lower due to charge trapping in the 2D material or its interface. (c) Benchmarking of monolayer MoS₂ transistors I_{on} vs. channel length (L) at $V_{DS} = 1 \text{ V}$.^{5,16,43,68,73-78} Also shown are IRDS high-performance (HP) and low-power (LP) metrics at $V_{DS} = 0.75 \text{ V}$ and 10-20 nm gate lengths.⁹ The simple model (solid lines) estimates achievable I_{on} with $R_C = 480 \Omega \cdot \mu\text{m}$ (this work) or $1 \text{ k}\Omega \cdot \mu\text{m}$. The low R_C achieved in this work (or lower) is needed to meet IRDS-HP metrics at reduced channel lengths. The data points are meant to be representative and not exhaustive. A more complete data set is available on our 2D transistor benchmarking website.⁵⁸

Supporting Information for:

High Current Density in Monolayer MoS₂ Doped by AlO_x

Connor J. McClellan¹, Eilam Yalon^{1,2}, Kirby K.H. Smithe¹, Saurabh V. Suryavanshi¹, and Eric Pop^{1,3,*}

¹Electrical Engineering, Stanford University, Stanford, CA 94305, USA

²Present address: Electrical Engineering, Technion, Israel Institute of Technology, Haifa, 32000, Israel

³Materials Science and Engineering, Stanford University, Stanford, CA 94305, USA

*Corresponding author: epop@stanford.edu

Section S1. Raman and PL Data on Doping

We used Raman spectroscopy and photoluminescence (PL) measurements for initial characterization of AlO_x-doped MoS₂. Figure 1d from the main text displays Raman spectra of MoS₂ before and after doping with the AlO_x encapsulation layer. We observe red-shifts in both the E' and A₁' peaks after AlO_x deposition. The A₁' peak is expected to red-shift with increasing carrier concentration of MoS₂,¹ and the observed 0.7 cm⁻¹ shift corresponds to induced carrier density $\Delta n \sim 3.2 \times 10^{12}$ cm⁻², lower than $\Delta n \sim 8.6 \times 10^{12}$ cm⁻² obtained by electrical characterization. However, we note the electrical measurement is more accurate than the Raman estimate, due to the limited spectrometer resolution.

The E' peak of monolayer (1L) MoS₂ is sensitive to strain² but its asymmetry seen in main text Fig. 1d is consistent with a doping-induced Fano effect, which has been previously noted in several other semiconductors with high doping.^{3,4} Raman measurements of MoS₂ capped by 150°C ALD-deposited AlO_x *without* the Al seed layer (Fig. S1) show no shift of the A₁' peak and no asymmetry of the E' peak, suggesting that the doping effect is enhanced with the Al seed layer (which subsequently oxidizes) for conformal deposition of AlO_x and doping of the underlying MoS₂.

PL measurements in main text Fig. 1c show a decrease and slight red shift of MoS₂ PL after AlO_x capping. The shift is consistent with the effects of tensile strain² and dielectric screening⁵ that decrease the MoS₂ optical band gap. In addition, the broadening of the PL peak indicates higher rate of non-radiative recombination, ostensibly due to the presence of charge and defects in the AlO_x.

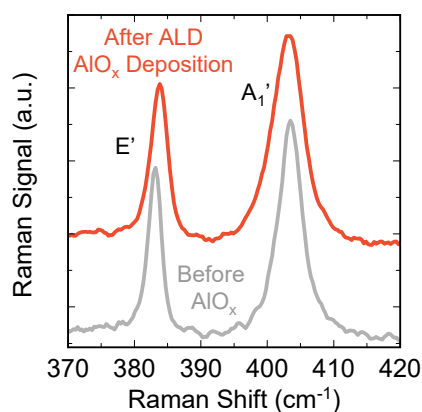


Fig. S1 Raman Spectra. Raman spectra of bare MoS₂ before AlO_x and after 150°C ALD-AlO_x deposition *without* Al seeding layer. Contrasting with the Raman spectra in main text Fig. 1d, not using the Al seeding layer causes no change in the A₁' peak and no Fano asymmetry of the E' peak.

Section S2. Extraction of Interface Trap Density from Change in Subthreshold Swing

We estimate the interface trap density (D_{it}) with the standard model of subthreshold current in field-effect transistors (FETs), aided by the diagram in Fig. S2. The subthreshold swing is:^{6,7}

$$SS \approx (\ln 10) \frac{k_B T}{q} \left(1 + \frac{C_{it} + C_q}{C_{ox}} \right) \quad (E1)$$

where k_B is the Boltzmann constant, T is the temperature, q is the elementary charge, C_{it} is the interface trap capacitance ($C_{it} = q^2 D_{it}$), C_q is the MoS₂ quantum capacitance, and C_{ox} is the oxide capacitance ($C_{ox} = \epsilon_{ox}/t_{ox} \approx 115$ nF/cm² for our 30 nm SiO₂ back-gate oxide). We ignore the depletion capacitance ($C_D = \epsilon_{MoS2}/t_{mos2}$) for monolayer MoS₂, as it will be much larger than the series C_q and C_{it} . As the Al deposition (on top) will not affect C_{ox} (bottom) or C_q , we can approximate the change in D_{it} due to AlO_x capping of MoS₂ from the change in SS , resulting in:

$$\Delta D_{it} \approx \frac{\Delta SS \times C_{ox}}{(\ln 10) k_B T} \quad (E2)$$

This equation stipulates that the SS of MoS₂ FETs depends on the interface trap density (D_{it}), but is independent of the mobile charge concentration and should not change with doping.

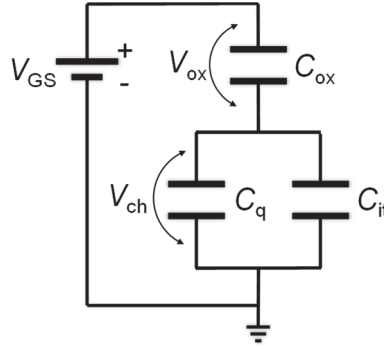


Fig. S2. MoS₂ FET Capacitance Schematic. Circuit schematic of the monolayer MoS₂ transistor including quantum capacitance (C_q) and interface trap capacitance (C_{it}) effects on the gate control. V_{ch} and V_{ox} are the voltages dropped across the channel and oxide, respectively.

Section S3. Modeling of Charge Trapping and Charge Doping

To illustrate the difference between trapping and doping, we use a drift-diffusion model⁶ to capture the transfer characteristics of a 2D n -type FET with both interface traps and doping. The classical drift current⁷ in the linear region describes electron motion from source to drain:

$$I_{drift} = qn v_d \quad (E3)$$

$$n = C_{ox} \left(V_{GS} - V_T - \frac{V_{DS}}{2} \right) / q \quad (E4)$$

$$v_d = \frac{\mu_{eff} F}{\left[1 + \left(\frac{\mu_{eff} F}{v_{sat}} \right)^\gamma \right]^{1/\gamma}} \quad (E5)$$

where V_T is the threshold voltage, n is the average electron density between source and drain, v_d is the average drift velocity in the MoS₂ channel, F is the average lateral field $F \approx (V_{DS} - 2I_D R_C)/L$, v_{sat} is the saturation velocity of MoS₂ ($\approx 4 \times 10^6$ cm/s), γ is an empirical fitting parameter ($\gamma \approx 5$) and μ_{eff} is the effective electron mobility.⁸

However, modeling the subthreshold diffusion current is difficult in a monolayer 2D transistor, as the depletion capacitance is large and the quantum capacitance (C_q) dominates. Ref. 9 gave equations for

C_q with a known Fermi energy (E_F), although E_F is not easily estimated in experimental devices. As our goal is modeling the effects of traps on the change in subthreshold current, we estimate C_q from the undoped 2D FET using eq. E1 over a V_{GS} range, and then calculate E_F using Ref. 9. With the extracted E_F for the undoped MoS₂ FET, we then incorporate trap levels with delta distributions in computing C_q using eq. 4 of Suryavanshi *et al.*⁶ Thus, the subthreshold diffusion current is:

$$I_{\text{diff}} = \frac{qD_n N_{2D}}{L} \ln \left(\frac{\exp \left[\frac{q(V_{GS} - V_T)}{C_r k_B T} \right] + 1}{\exp \left[\frac{q(V_{GS} - V_T - V_{DS})}{C_r k_B T} \right] + 1} \right) \quad (\text{E6})$$

where $D_n = (k_B T/q)\mu_{\text{eff}}$ is the electron diffusion coefficient, N_{2D} is the 2D density of states from equation 2 of Suryavanshi *et al.*⁶ and C_r is the normalized capacitance term [$C_r = 1 + (C_q + C_{it})/C_{\text{ox}}$]. The total current is then simply $I_D = I_{\text{drift}} + I_{\text{diff}}$ from equations (E3) and (E6) above.

For the simulations shown in the main text Fig. 2 we use the following parameters, also labeled on Fig. S3. For the initial MoS₂ device without AlO_x capping we use $V_T = 10$ V, $\mu_{\text{eff}} = 33$ cm²V⁻¹s⁻¹, and a native interface trap density $D_{it} = 5 \times 10^{12}$ cm⁻²eV⁻¹ at an energy level $E_{it} = -100$ meV (i.e. 100 meV below the MoS₂ conduction band) to capture the traps already present within the CVD-grown MoS₂ or at the SiO₂/MoS₂ interface. This D_{it} at $E_{it} = -100$ meV is present in all our simulations, as these traps remain at the SiO₂/MoS₂ interface.

After deposition of AlO_x, we add two trap levels at $E_{it} = -200$ meV and -50 meV, each with $D_{it} = 2.5 \times 10^{13}$ cm⁻²eV⁻¹ without changing other model parameters (i.e. constant V_T and μ_{eff}). To model the channel after 200°C annealing in N₂, we remove the trap levels from $E_{it} = -200$ meV and -50 meV, but add an additional trap level at $E_{it} = 250$ meV (above the conduction band) with $D_{it} = 7 \times 10^{12}$ cm⁻²eV⁻¹. These parameters are listed on and correspond to the three scenarios labeled in Fig. S3.

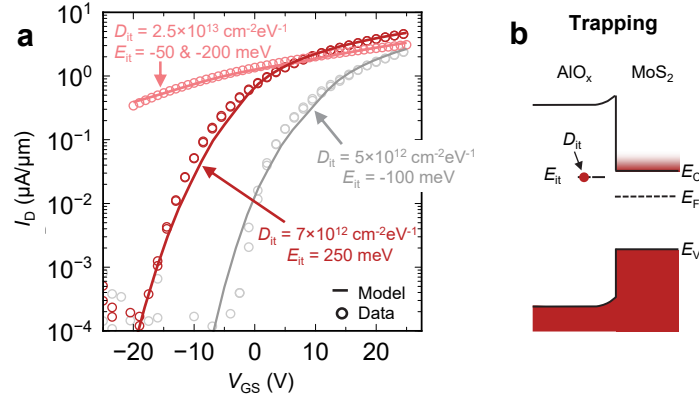


Fig. S3. Experimental I - V and Trap Modeling. (a) Measured I_D vs. back-gate V_{GS} (symbols) shown in main text Fig. 2b. Simulations (lines) are shown with parameters used. Colors are consistent with Fig. 2 in the main text: (1) gray is the bare MoS₂ device before AlO_x deposition, (2) light red is right after deposition, and (3) dark red is after the anneal step. We note the negative threshold voltage shift after AlO_x deposition (due to doping), and the recovery of the good on/off ratio after the anneal step. (b) Band diagram showing E_{it} and D_{it} in the AlO_x on MoS₂ in the trapping state, i.e. E_{it} within the MoS₂ band gap. The charge trap distribution is incorporated in the model as a delta function $D_{it}\delta(E-E_{it})$, as described by Suryavanshi *et al.*⁶

Section S4. Top-Gate Measurements with Doping AlO_x Layer

We also evaluate the AlO_x capping layer as a top-gate dielectric (Fig. S4a). The double-gate transistor has a source-drain contact separation $L = 6$ μm , top gate length $L_G = 5$ μm , and channel width $W = 3$ μm , confirmed by atomic force microscopy (AFM). The Pd top-gate was defined using electron beam lithography and deposited with electron-beam evaporation. After the electron-beam evaporation step,

we observed that all devices on the sample displayed trapping-like characteristics (Fig. S4b). The degradation of top-gate control originates from an increase in the density of mid-gap defect states due to oxide damage induced by the high energy X-rays emitted during electron-beam evaporation.^{10,11} However, a 40 min 200°C N₂ anneal recovers the gate control to the “doping” state (Fig. S4b).

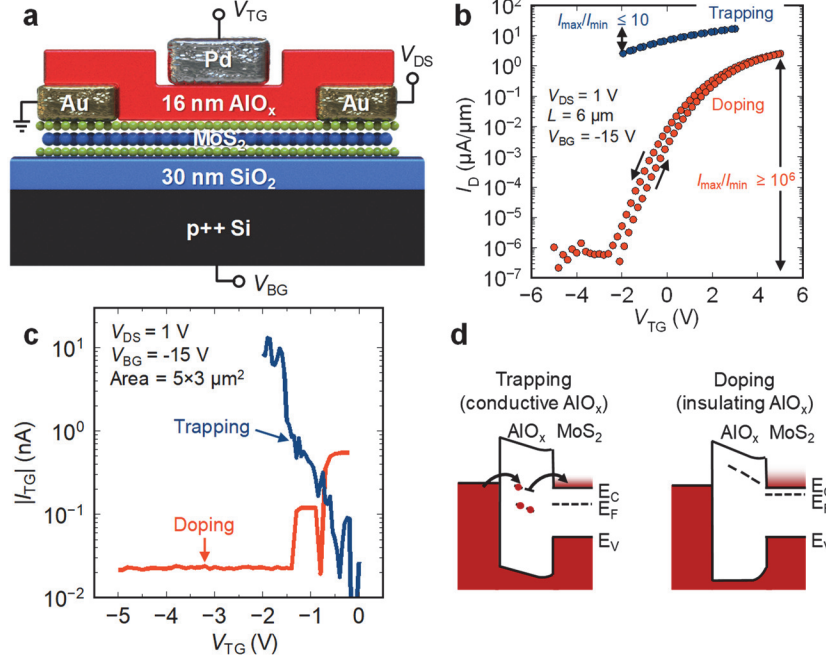


Fig. S4. Top-Gate Measurements: (a) Schematic of dual-gated MoS₂ FET, using the AlO_x layer as a top-gate dielectric. (b) Measured I_D vs. V_{TG} data showing the large I_{on}/I_{off} of the doping state and small I_{on}/I_{off} of the trapping state, similar to data using the back-gate. The arrows mark forward and backward sweeps, indicating relatively low hysteresis. (c) Top-gate leakage measurements showing that the AlO_x dielectric with a large trap concentration (“trapping”) is more conductive than with low trap concentration (“doping”). (d) Energy band diagram showing how mid-gap traps in the AlO_x lead to trap-assisted tunneling and high gate leakage, but higher-energy state traps (in the “doping” state of the oxide) do not.

Fig. S4c displays the measured top-gate leakage current (I_{TG}) for the trapping and doping states. Large I_{TG} is measured for the trapping state, limiting the top-gate voltage (V_{TG}) sweep from only -2 V to 3 V in Fig. S4b. For the doping state, I_{TG} is reduced to <10 pA, allowing for a V_{TG} sweep from -5 V to 5 V. The large contrast in I_{TG} between trapping and doping offers insight into the state of the AlO_x in these two cases, illustrated with schematic energy band diagrams in Fig. S4d. AlO_x in the trapping state is leaky due to defects that promote electron conduction and trap MoS₂ electrons, degrading FET performance and increasing I_{TG} by trap-assisted tunneling. AlO_x in the doping state has higher defect energy levels, above the MoS₂ conduction band, reducing trap-assisted tunneling and decreasing I_{TG} . The lower I_{TG} indicates that post-anneal AlO_x can be effectively used to dope the underlying 2D semiconductor while also serving as a top-gate dielectric, allowing for process integration of doping and dielectric formation. However, future studies will need to reduce the physical (and equivalent) oxide thickness of the top-gate dielectric, and/or combine it with an additional layer which has a higher dielectric constant (e.g. HfO₂). This is needed to reduce the operating gate voltage of MoS₂ transistors.

Section S5. Transfer Length Method Measurements

We use the transfer length method (TLM)¹² to obtain both sheet and contact resistance of our MoS₂ after doping with the AlO_x capping layer. Fig. S5a shows a TLM structure with six channel lengths of

180, 280, 380, 480, 680, and 980 nm (measured by AFM). Fig. S5b plots the total measured resistance (R_{tot}) vs. channel length (L), showing the expected linear scaling. The sheet resistance (R_{sh}) and contact resistance (R_{C}) are extracted from the slope and vertical intercept of the TLM plot as:

$$R_{\text{tot}} = R_{\text{sh}}L + 2R_{\text{C}}. \quad (\text{E7})$$

With the extracted R_{sh} , the effective mobility (μ_{eff}) is obtained as:

$$\mu_{\text{eff}} = (qnR_{\text{sh}})^{-1} \quad (\text{E8})$$

where the carrier density n is estimated from the gate voltage in eq. E4. We note that due to uncertainties in the threshold voltage V_{T} (and due to small contributions from $C_{\text{q}} \leq 5\%$ at $n \geq 5 \times 10^{12} \text{ cm}^{-2}$) the carrier density n and therefore the mobility are more accurately estimated at larger V_{GS} . There are also small V_{T} variations between the different channels within the TLM structure, and thus the TLM extraction is performed at the same gate overdrive ($V_{\text{GS}} - V_{\text{T}}$) for each individual channel. Additional details of TLM extraction, uncertainty estimates, and other pitfalls are given in English *et al.*¹²

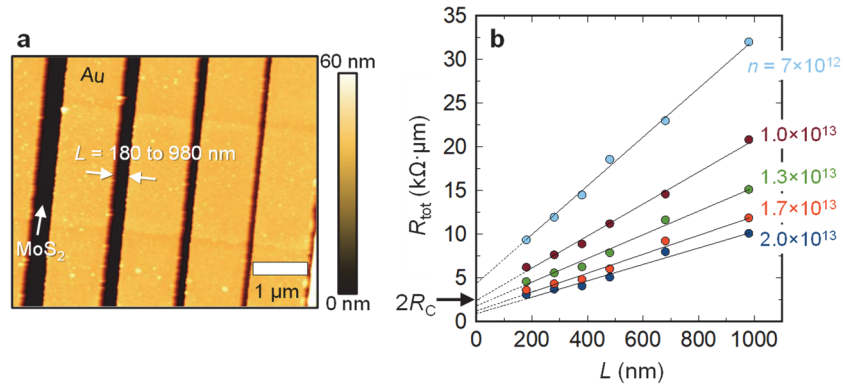


Fig. S5. TLM Measurements: (a) AFM of TLM structure on monolayer MoS₂, from main text Fig. 1b. (b) Measured R_{tot} vs. L , used for extracting R_{C} and R_{sh} at different carrier densities. All lengths were measured by SEM and AFM, confirming channel lengths ~ 20 nm smaller than target values (i.e. $L = 980$ nm, 680 nm, 480 nm, etc.). The 380 nm channel had slightly better characteristics than other channel lengths (i.e. lower V_{T}) while 680 nm was slightly worse, causing some of the uncertainty in the R_{C} extraction.

The effective mobility μ_{eff} may be underestimated vs. the Hall mobility because the extraction of n may be overestimated due to traps in the MoS₂ and/or surrounding dielectrics,^{13,14} as discussed in the main text. However, μ_{eff} is an effective mobility that captures how well the gate controls R_{sh} of the MoS₂ (independent of R_{C}), and is also used to calculate the current with eqs. E3-E5. Thus, μ_{eff} is the correct metric which captures the transconductance and net current flow in these transistors.

From the TLM data, we can also extract the current transfer length (L_{T}), which is the characteristic distance that electrons travel in the semiconductor under the metal contact before flowing up into the metal. This can be simply estimated as $L_{\text{T}} = R_{\text{C}}/R_{\text{sh,c}}$ where $R_{\text{sh,c}}$ is the sheet resistance of the MoS₂ under the contact.¹² For simplicity, we use our average channel $R_{\text{sh}} \approx 9 \text{ k}\Omega/\square$ but the actual $R_{\text{sh,c}}$ could be higher due to (some) metal evaporation damage to the MoS₂ under the metal contact. From this, we estimate an upper bound of $L_{\text{T}} = 53 \text{ nm}$ at $n = 2 \times 10^{13} \text{ cm}^{-2}$, indicating the contact length of our devices could be scaled to ~ 50 nm before contact current crowding effects become non-negligible.

Section S6. High On-Current and High On/Off

While achieving high drain current in transistors can decrease circuit delay, transistors must also have a high $I_{\text{on}}/I_{\text{off}}$ ratio to maintain low leakage current. Fig. S6 plots the measured log-scale I_{D} vs. V_{GS} of a doped MoS₂ FET showing $I_{\text{on}}/I_{\text{off}} > 10^6$ at both $V_{\text{DS}} = 2 \text{ V}$ and 5 V . These results contrast many

previous reports of high current in 2D material transistors, where increasing lateral field (i.e. V_{DS}) results in an exponential increase in I_{off} , reducing I_{on}/I_{off} . The increase in I_{off} is common in small band gap material transistors, such as black phosphorus, where larger lateral field increases band-to-band leakage current. Our devices can maintain a high I_{on}/I_{off} as monolayer MoS₂ has a larger band gap ($E_G > 2$ eV)¹⁵ reducing band-to-band tunneling effects.

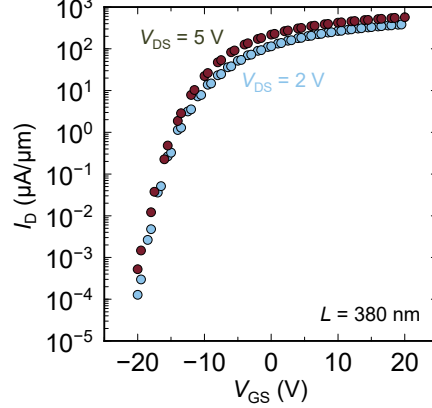


Fig. S6. High-Current I_D - V_{GS} : Measured log I_D vs. V_{GS} of a highly doped MoS₂ FET showing $I_{on}/I_{off} > 10^6$ at $V_{DS} = 2$ V and 5 V. The channel length $L = 380$ nm and back-gate oxide thickness $t_{ox} = 30$ nm.

Section S7. Thermal Modeling of MoS₂ FETs

We use a compact thermal model of 2D material FETs to estimate the effects of self-heating on device performance. We first calculate the thermal conductance per unit length (g) and thermal resistance (R_{th}) from MoS₂ to the Si substrate back-side from the equations:⁶

$$g = \frac{R_{Cox}}{W} + \left\{ \frac{\pi\kappa_{ox}}{\ln\left[6\left(\frac{t_{ox}}{W}+1\right)\right]} + \frac{\kappa_{ox}}{t_{ox}}W \right\}^{-1} + \frac{1}{2\kappa_{si}} \left(\frac{L}{W_{eff}}\right)^{\frac{1}{2}} \quad (E9)$$

$$R_{th} = \frac{1}{gL} \quad (E10)$$

where R_{Cox} is the thermal boundary resistance between MoS₂ and SiO₂, W is the width of the MoS₂ channel, κ_{ox} is the thermal conductivity of SiO₂, t_{ox} is the thickness of the SiO₂, κ_{si} is the thermal conductivity of the highly doped Si substrate, W_{eff} is the effective width of the MoS₂ device including thermal spreading¹⁶ into the SiO₂ ($W_{eff} \approx W + 2t_{ox}$) and L is the length of the MoS₂ channel. With an estimation of R_{th} , the increase in temperature can be expressed as:

$$T_{avg} = T_0 + PR_{th} \left\{ \frac{1+gL_H R_{Tx} - 2xL_H/L}{1+gL_H R_{Tx}} \right\} \quad (E11)$$

where T_0 is the ambient temperature (~ 295 K for our measurements unless otherwise stated), P is the input power [corrected for the voltage drop across the contacts, $P = I_D(V_{DS} - 2I_D R_C)$], R_T is the thermal resistance into the 35 nm thick Au contacts,¹⁶ $x = \tanh[L/(2L_H)]$, and L_H is the thermal healing length along the MoS₂ and to the metal contacts. We estimate $L_H \approx 110$ nm using the equation:

$$L_H = \sqrt{\kappa_{eff} t_{MoS2} \left(\frac{W}{g} + R_{Cox}\right)}, \quad (E12)$$

where $\kappa_{eff} = \kappa_{MoS2} + \kappa_{cap}(t_{cap}/t_{MoS2})$ is the effective lateral thermal conductivity¹⁷ accounting for parallel heat flow along the MoS₂ and the AlO_x capping layer ($t_{cap} \approx 15$ nm and $\kappa_{cap} \approx 3$ Wm⁻¹K⁻¹).¹⁸ Thus, the thermal model includes both heat sinking to the substrate (most important in longer channels, $L > 3L_H \sim 330$ nm) and heat sinking to the contacts (more important in the shorter channels, $L < 3L_H \sim 330$ nm). Additional details about this thermal model can be found in previous work.^{6,8,17}

Parameter	Value	Reference
R_{Cox}	$7 \times 10^{-8} \text{ m}^2 \text{KW}^{-1}$	19
κ_{ox}	$1.3 \text{ Wm}^{-1} \text{K}^{-1}$	20
κ_{si}	$95 \text{ Wm}^{-1} \text{K}^{-1}$	19
κ_{MoS_2}	$34 \text{ Wm}^{-1} \text{K}^{-1}$	21

Table S1. Thermal Parameters used for our calculations, all near 300 K. R_{Cox} is thermal boundary resistance, i.e. the inverse of the thermal boundary conductance (TBC). The thermal conductivity of silicon (κ_{si}) corresponds to our highly doped substrates, as measured in Yalon *et al.*¹⁹

The effect of temperature on the I - V characteristics is included through:

$$\mu_{\text{eff}} = \mu_0 \left(\frac{T}{T_0} \right)^\beta \quad (\text{E13})$$

where $\beta = -1.24$ is extracted from temperature-dependent measurements of MoS₂ mobility⁸ and μ_0 is the effective mobility at 295 K ($\sim 33 \text{ cm}^2 \text{V}^{-1} \text{s}^{-1}$ is this work). For thermal conductivities and boundary resistances, we used the values listed in Table S1. The model results shown in the main text Fig. 4 demonstrate how self-heating can significantly limit the on-state current. Thus, improved heatsinking will reduce mobility degradation and velocity saturation,⁸ improving overall device performance.

We also estimate the performance of our devices with a $3 \times$ reduction of thermal boundary resistance ($R_{\text{Cox}}/3$) in Fig. S7. The maximum I_{on} increases to $930 \text{ } \mu\text{A}/\mu\text{m}$ at $n = 2 \times 10^{13} \text{ cm}^{-2}$ and $V_{\text{DS}} = 5 \text{ V}$, as the max temperature decreases from 700 K to 500 K with the improved heatsinking. There is also a more linear increase in current with V_{GS} as the device approaches the v_{sat} -limited regime and the current saturation is less dominated by self-heating. Improvement in device thermal resistance can be achieved by using more thermally conductive dielectrics (e.g. h-BN, AlN)²² or improved thermal interfaces (lower R_{Cox}), because the intrinsic thermal conductivity of the MoS₂ plays only a small role. Although shorter channel transistors will have higher power density, decreasing the channel length ($L < 3L_{\text{H}}$) should reduce the overall self-heating by increasing heat sinking to the contacts.

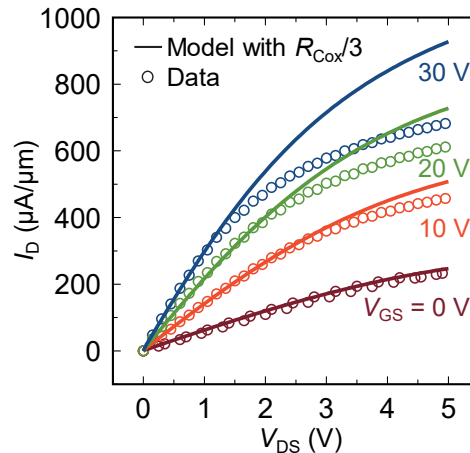


Fig. S7. Model with Improved Heat Sinking. Measured I_{D} vs. V_{DS} data (symbols) of a high-current monolayer MoS₂ FET ($L = 380 \text{ nm}$) and simulations (lines) showing that reducing the MoS₂-SiO₂ thermal boundary resistance (R_{Cox}) increases the maximum current drive by reducing self-heating. R_{Cox} was reduced from $7 \times 10^{-8} \text{ m}^2 \text{KW}^{-1}$ (default parameter in Table S1) to $2.3 \times 10^{-8} \text{ m}^2 \text{KW}^{-1}$, corresponding to increased thermal boundary conductance ($\text{TBC} = 1/R_{\text{Cox}}$) from $14.3 \text{ MWm}^{-2} \text{K}^{-1}$ to $43 \text{ MWm}^{-2} \text{K}^{-1}$.

Section S8. Effect of Al Seed layer on Doping

We also studied the effect of electron-beam physical vapor deposited (EBPVD) Al layers on our CVD-grown monolayer MoS₂ FETs. We deposited a series of 1.5 nm layers of Al at a pressure of 10⁻⁶ Torr on MoS₂ FETs, exposing the Al to atmosphere for several hours and measuring the electrical characteristics (in a vacuum probe station) between each Al deposition. From previous studies,²³ we know the thin layer of EBPVD Al will completely oxidize upon air exposure, forming a sub-stoichiometric AlO_x compound. Thus, this AlO_x layer capping the MoS₂ channel is not conductive, and the current is entirely carried by the MoS₂.

Fig. S8 shows the *n*-type doping effect of the thin AlO_x layers on the electrical characteristics of the MoS₂ FET after the first two 1.5 nm of Al depositions (1.5 nm and 3 nm). However, after further Al depositions (4.5 nm and 6 nm), we see a *decrease* in MoS₂ conductivity as the AlO_x doping effect begins to degrade from continued exposure to air. We believe this degradation in conductivity results from carbon contamination on the AlO_x surface and decrease in the fixed charge doping density in the AlO_x layers.²⁴ This degradation in device performance with Al seeding alone contrasts the stable doping observed with seed layer *followed* by ALD-deposited AlO_x, as the higher quality and thicker ALD AlO_x prevents carbon contamination to the AlO_x/MoS₂ interface. Thus, we conclude that a thin (sub-3 nm) seed layer of Al is necessary but not sufficient to induce the maximum doping effect observed in our MoS₂ devices.

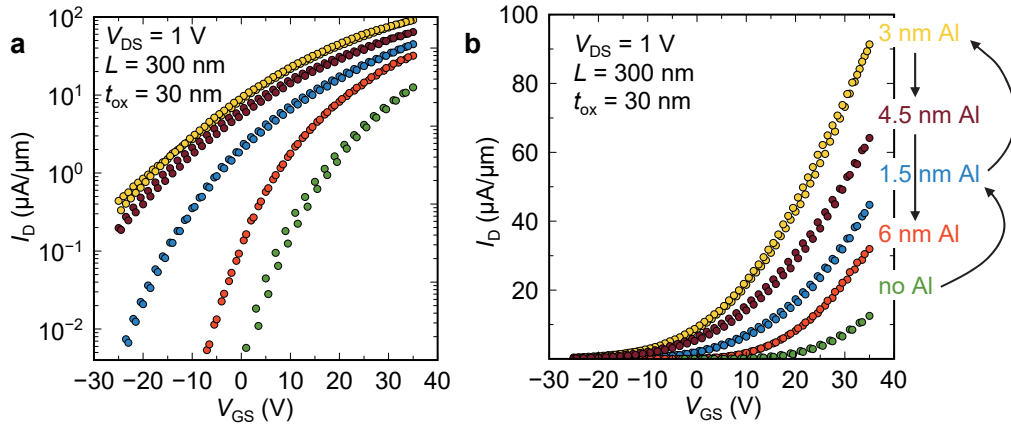


Fig. S8. Effect of Al Seed Layer. Measured (a) log and (b) linear scale I_D vs. V_{GS} of an MoS₂ device after a series of Al seed layer depositions (see arrows), showing increase in conductivity from no Al to 1.5 and 3 nm of Al. However, after 4.5 and 6 nm of Al, the conductivity degrades, likely due to surface contamination. The sample is exposed to air after each deposition round, ensuring the AlO_x formed is not conducting. Double sweeps (forward and backward) are shown for each data set, revealing minimal hysteresis.

Section S9. H₂ Annealing to Increase Defects

While N₂ annealing can reduce MoS₂/AlO_x interface traps, we found that H₂ annealing can increase the interface traps. Fig. S9 demonstrates how the doping concentration can be further increased by a combination of H₂ and N₂ anneals on an MoS₂ device doped with 15 nm ALD-capped AlO_x. H₂ anneals promote the generation of oxygen vacancies in AlO_x by reacting with oxygen and reducing AlO_x.²⁵ After a 30 minute 150°C Ar/H₂ anneal (5% H₂), the measured I_D vs. V_{GS} shows trapping, as indicated by the significant increase in SS. An N₂ anneal increases the trap energy levels, shifting the V_T by -10 V (to more negative values) and increasing the induced carrier concentration by $\Delta n \sim 6 \times 10^{12} \text{ cm}^{-2}$ compared to the FET before H₂ annealing.

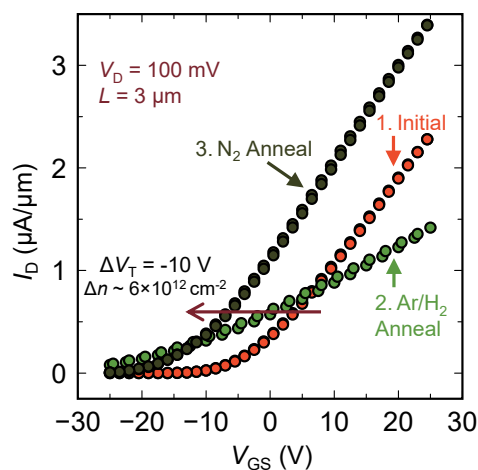


Fig. S9. H₂ Annealing: Measured I_D vs. V_{GS} data of a MoS₂ device doped by ~15 nm ALD-deposited AlO_x capping before treatment, after Ar/H₂ annealing, and after N₂ annealing. A clear negative threshold voltage V_T shift is observed, indicating the series of Ar/H₂ and N₂ anneals can increase doping.

References

- 1 Chakraborty, B., Bera, A., Muthu, D., Bhowmick, S., Waghmare, U. V. & Sood, A. K., Symmetry-Dependent Phonon Renormalization in Monolayer MoS₂ Transistor. *Physical Review B* **2012**, 85 (16), 161403.
- 2 Conley, H. J., Wang, B., Ziegler, J. I., Haglund, R. F., Pantelides, S. T. & Bolotin, K. I., Bandgap Engineering of Strained Monolayer and Bilayer MoS₂. *Nano Lett.* **2013**, 13 (8), 3626-3630.
- 3 Chandrasekhar, M., Renucci, J. & Cardona, M., Effects of Interband Excitations on Raman Phonons in Heavily Doped N-Si. *Physical Review B* **1978**, 17 (4), 1623.
- 4 Tsang, J., Freitag, M., Perebeinos, V., Liu, J. & Avouris, P., Doping and Phonon Renormalization in Carbon Nanotubes. *Nature Nanotech.* **2007**, 2 (11), 725-730.
- 5 Lin, Y. X., Ling, X., Yu, L. L., Huang, S. X., Hsu, A. L., Lee, Y. H., Kong, J., Dressehaus, M. S. & Palacios, T., Dielectric Screening of Excitons and Trions in Single-Layer MoS₂. *Nano Lett.* **2014**, 14 (10), 5569-5576.
- 6 Suryavanshi, S. V. & Pop, E., S2DS: Physics-Based Compact Model for Circuit Simulation of Two-Dimensional Semiconductor Devices Including Non-Idealities. *Journal of Applied Physics* **2016**, 120 (22), 224503.
- 7 Streetman, B. & Banerjee, S. *Solid State Electronic Devices*. 6 edn, 311 (Prentice Hall, 2005).
- 8 Smithe, K. K., English, C. D., Suryavanshi, S. V. & Pop, E., High-Field Transport and Velocity Saturation in Synthetic Monolayer MoS₂. *Nano Lett.* **2018**, 18 (7), 4516-4522.
- 9 Ma, N. & Jena, D., Carrier Statistics and Quantum Capacitance Effects on Mobility Extraction in Two-Dimensional Crystal Semiconductor Field-Effect Transistors. *2D Materials* **2015**, 2 (1), 015003.
- 10 Shaneyfelt, M., Fleetwood, D., Schwank, J. & Hughes, K., Charge Yield for Cobalt-60 and 10-Kev X-Ray Irradiations of MOS Devices. *IEEE Trans. Nuclear Science* **1991**, 38 (6), 1187-1194.
- 11 Benedetto, J. M. & Boesch, H., The Relationship between ⁶⁰Co and 10-Kev X-Ray Damage in MOS Devices. *IEEE Transactions on Nuclear Science* **1986**, 33 (6), 1317-1323.
- 12 English, C. D., Shine, G., Dorgan, V. E., Saraswat, K. C. & Pop, E., Improved Contacts to MoS₂ Transistors by Ultra-High Vacuum Metal Deposition. *Nano Lett.* **2016**, 16 (6), 3824-3830.
- 13 Kim, T., Hur, J.-H. & Jeon, S., Pulse I-V Characterization of a Nano-Crystalline Oxide Device with Sub-Gap Density of States. *Nanotechnology* **2016**, 27 (21), 215203.

- 14 Kim, T., Choi, R. & Jeon, S., Influence of Fast Charging on Accuracy of Mobility in a-InHfZnO Thin-Film Transistor. *IEEE Electron Device Letters* **2016**, *38* (2), 203-206.
- 15 Hill, H. M., Rigosi, A. F., Rim, K. T., Flynn, G. W. & Heinz, T. F., Band Alignment in MoS₂/WS₂ Transition Metal Dichalcogenide Heterostructures Probed by Scanning Tunneling Microscopy and Spectroscopy. *Nano Lett.* **2016**, *16* (8), 4831-4837.
- 16 Liao, A. D., Wu, J. Z., Wang, X., Tahy, K., Jena, D., Dai, H. & Pop, E., Thermally Limited Current Carrying Ability of Graphene Nanoribbons. *Physical review letters* **2011**, *106* (25), 256801.
- 17 Mleczko, M. J., Xu, R. L., Okabe, K., Kuo, H.-H., Fisher, I. R., Wong, H.-S. P., Nishi, Y. & Pop, E., High Current Density and Low Thermal Conductivity of Atomically Thin Semimetallic WTe₂. *ACS Nano* **2016**, *10* (8), 7507-7514.
- 18 Cappella, A., Battaglia, J. L., Schick, V., Kusiak, A., Lamperti, A., Wiemer, C. & Hay, B., High Temperature Thermal Conductivity of Amorphous Al₂O₃ Thin Films Grown by Low Temperature Ald. *Advanced Engineering Materials* **2013**, *15* (11), 1046-1050.
- 19 Yalon, E., McClellan, C. J., Smithe, K. K., Muñoz Rojo, M., Xu, R. L., Suryavanshi, S. V., Gabourie, A. J., Neumann, C. M., Xiong, F., Farimani, A. B., & Pop, E., Energy Dissipation in Monolayer MoS₂ Electronics. *Nano Lett.* **2017**, *17* (6), 3429-2433.
- 20 Lee, S.-M. & Cahill, D. G., Heat Transport in Thin Dielectric Films. *Journal of Applied Physics* **1997**, *81* (6), 2590-2595.
- 21 Gabourie, A.J., Suryavanshi, S., Farimani, A.B., & Pop, E., Reduced Thermal Conductivity of Supported and Encased Monolayer and Bilayer MoS₂. *2D Materials* **2021**, *8*, 011001.
- 22 Xu, R. L., Muñoz Rojo, M., Islam, S., Sood, A., Vareskic, B., Katre, A., Mingo, N., Goodson, K. E., Xing, H. G., Jena, D. & Pop, E., Thermal Conductivity of Crystalline AlN and the Influence of Atomic-Scale Defects. *Journal of Applied Physics* **2019**, *126* (18), 185105.
- 23 English, C. D., Smithe, K. K., Xu, R. L. & Pop, E. Approaching Ballistic Transport in Monolayer MoS₂ Transistors with Self-Aligned 10 nm Top Gates. *2016 IEEE International Electron Devices Meeting (IEDM)*. **2016** 5.6. 1-5.6. 4.
- 24 Leonhardt, A., Chiappe, D., Afanas'ev, V. V., El Kazzi, S., Shlyakhov, I., Conard, T., Franquet, A., Huyghebaert, C. & De Gendt, S., Material-Selective Doping of 2D TMDC through Al_xO_y Encapsulation. *ACS Applied Materials & Interfaces* **2019**, *11* (45), 42697-42707.
- 25 Braaten, O., Kjekshus, A. & Kvande, H., The Possible Reduction of Alumina to Aluminum Using Hydrogen. *JOM* **2000**, *52* (2), 47-53.